Master thesis

Search for multi-strange dibaryons in pp and p-Pb collisions at ALICE

M201128 Ryoka Tokumoto

Quark Physics Laboratory

Graduate School of Advanced Science and Engineering
Physics Program, Hiroshima University

SuperVisor　Professor : Kenta Shigaki

Chief Examiner　Associate Professor : Yorito Yamaguchi

Vice Examiner　Professor : Takuya Morozumi
Professor : Satoru Endo

January 31, 2022

Abstract

Quarks, the smallest element of matter, cannot exist as a free particle. Quarks have a color charge and are confined inside color-neutral composite particles such as baryons consisting of three quarks. Quantum chromodynamics (QCD), the fundamental theory of strong interactions, does not rule out the existence of exotic hadrons. The exotic hadrons consisting of six quarks are called as a dibaryons, particularly a dibaryons with multiple s quarks as multi-strange dibaryons, which are not discovered yet with certainty. Multi-strange dibaryons can lead to not only further understanding of QCD by showing a new hadronic form, but also providing an additional information on baryon-baryon interactions.

H dibaryon and $N\Omega$ dibaryon are leading candidates for multi-strange dibaryons because the Pauli blocking does not work and attractive forces between the two baryons, which are enough for dibaryon formation predicted by Lattice QCD calculations, have been observed. They are expected to have decay channels $H \rightarrow \Lambda\Lambda$, $p\Xi$ and $N\Omega \rightarrow \Lambda\Xi$. Thus, they can be directly searched by invariant mass reconstruction with decay particles.

The Large Hadron Collider (LHC) at the European Organization for Nuclear Research (CERN), the world's largest and most powerful particle accelerator, can produce abundance of baryons including multiple s quarks. We have searched for H dibaryon and $N\Omega$ dibaryon using the LHC Run 2 pp and p-Pb collision data obtained by the ALICE experiment. The invariant mass distributions of $\Lambda\Lambda, p\Xi, \Lambda\Xi$ have been obtained. Their possible signals have been evaluated based on the statistical hypothesis test, the CL_s calculation, with the obtained mass distributions. As a result, no significance above 2 σ uncertainty of the experimental sensitivity due to a statistical fluctuation is observed assuming the signal widths of $\Lambda\Lambda, p\Xi, \Lambda\Xi$ are 5, 10 and 20 MeV/c^2, respectively.

In conclusion, we did not find any evidence for the existence of the multi-strange dibaryons in this study.

Contents

List of figures

1 Introduction

1.1 Quantum Chromodynamics (QCD)

The protons and neutrons (nucleons) that make up matter are composed of three quarks, which are the smallest element of matter. The basic theory of the strong interaction between quarks is called QCD by comparing the fact that the stability of three quarks is similar to the three primary colors of light. QCD describes all the physical phenomena associated with strong interactions. Starting from the properties of quarks, it is possible to derive the properties of nucleons and even the nuclear force by using this theory. However, these calculations are not easy. This is because QCD has the property of asymptotic freedom, which means that the interaction becomes stronger in the low energy region. The coupling constant α_s for QCD is expressed as a function of the momentum transfer Q in Eq.1.1, where n_q is the number of quark types and Λ_{QCD} is the momentum scale that characterizes the coupling strength.

$$\alpha_s(Q) \simeq \frac{12\pi}{(32 - 2n_q)\ln\left(Q^2/\Lambda^2_{\mathrm{QCD}}\right)} \tag{1.1}$$

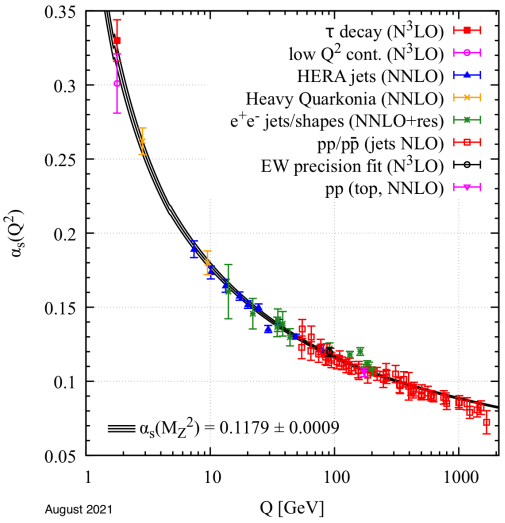

Fig. 1.1: QCD coupling constant $\alpha_s(Q)$ [1]

Fig.1.1 shows the momentum scale dependence of α_s. It shows the values of α_s measured for various reactions as a function of the scale Q for that reaction. The black curve is the result of a theoretical calculation, showing that the theory agrees well with the data. In the high energy region (short range region) where Q is sufficiently large compared to $\Lambda_{\rm QCD}$, α_s becomes sufficiently small. Therefore, it can be described by perturbation theory. On the other hand, the perturbation expansion does not converge due to the increase of α_s in the low energy region (long range region). Therefore, QCD cannot be described by perturbation theory. The most promising method for solving QCD in such low energies is lattice QCD. This is a method of solving approximate QCD on a lattice dividing 4-dimensional spacetime by numerical simulation. Recently, lattice QCD calculations using supercomputers have made it possible to study the color confinement mechanism of quarks and the interaction between hadrons.

1.2 Hadron picture

1.2.1 Quark model

Quarks cannot exist as a free particle and are captured inside hadrons, which are color-neutral composite particles. Hadrons are generally classified into baryons, which consist of three quarks, and mesons, which consist of two quarks. Baryons are fermions typified by nucleons. Mesons are bosons typified by π, the first meson predicted by Hideki Yukawa in 1935[2] and discovered by cosmic ray observation in 1947[3]. Later on, baryons such as K-meson, Λ, and Ξ with new quantum number Strangeness (S) were discovered one after another.

The discovery of these multiple hadrons led to the view that hadrons are composite particles made from elementary particles. Experimentally, the existence of quarks in hadrons was confirmed in the late 1960s by deep inelastic scattering, in which high-energy electrons collide with hadrons. The quark model[4] [5] was considered by Gell-Mann and Zweig in 1964 to systematically organize such various hadrons. According to the quark model, the properties of hadrons are determined by their constituent quarks. Each quark has a spin of 1/2 and a baryon number B = 1/3. In addition, the charge Q, the third component of isospin I_3, the strangeness S, and the hypercharge Y are given as additive quantum numbers. The relational expression for these quantum numbers is shown in Eq.1.2, 1.3, and this is called Gell-Mann-Nishijima formula.

$$Q = I_3 + \frac{Y}{2} \tag{1.2}$$

$$Y = B + S \tag{1.3}$$

The quark model explains well the origin of hadrons and their quantum numbers by using these quark quantum numbers.

Meson nonet

The mesons are assumed to be composed of $q\bar{q}$ (where q is a quark), and its total spin is 0 or 1. For the three flavors of quarks u, d, and s (flavor SU(3)), there are nine combinations (nonet).

$$3 \otimes \overline{3} = 8 \oplus 1 \tag{1.4}$$

This implies that the 9 states can be decomposed into a 8 dimensional irreducible representation and a 1 dimensional representation[6]. These can be represented as in Fig.1.2.

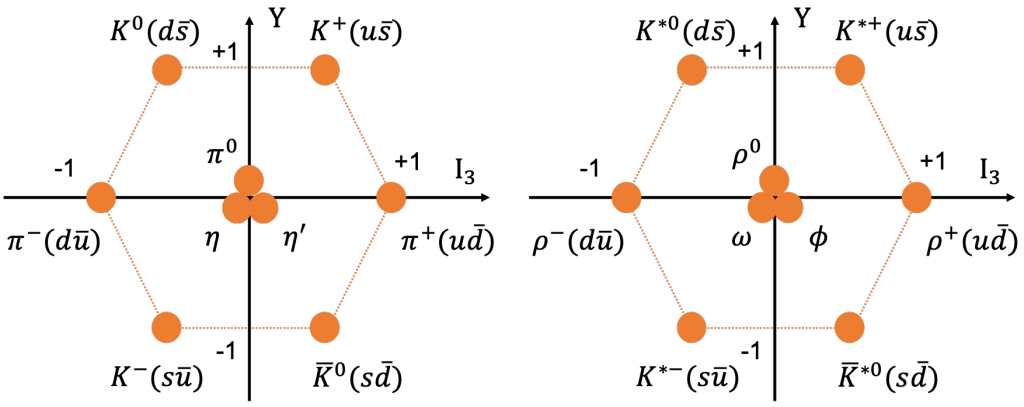

Fig. 1.2: (left) Pseudoscalar mesons in SU(3) (right) Vector mesons in SU(3)

Baryon decouplet and octet

A baryon in flavor SU(3) can be decomposed into a decouplet, octet, and a singlet as in Eq.1.5.

$$3 \otimes 3 \otimes 3 = 10 \oplus 8 \oplus 1 \tag{1.5}$$

Due to the SU(6) symmetry, which takes into account spin and flavor, the decouplet and octet are the ground states, i.e, there are 18 different baryons. These are represented as shown in the Fig 1.3. The total spin of the baryon is 1/2 or 3/2, and the mapping of the total angular momentum J and parity P to the decouplet and octet is as follows.

$$J^P = \frac{1}{2}^+ \; Baryonoctet \tag{1.6}$$

$$J^P = \frac{3}{2}^+ \; Baryondecouplet \tag{1.7}$$

In addition, Baryons with non-zero strangeness (Λ, Σ, Ξ, Ω, etc.) are called hyperons.

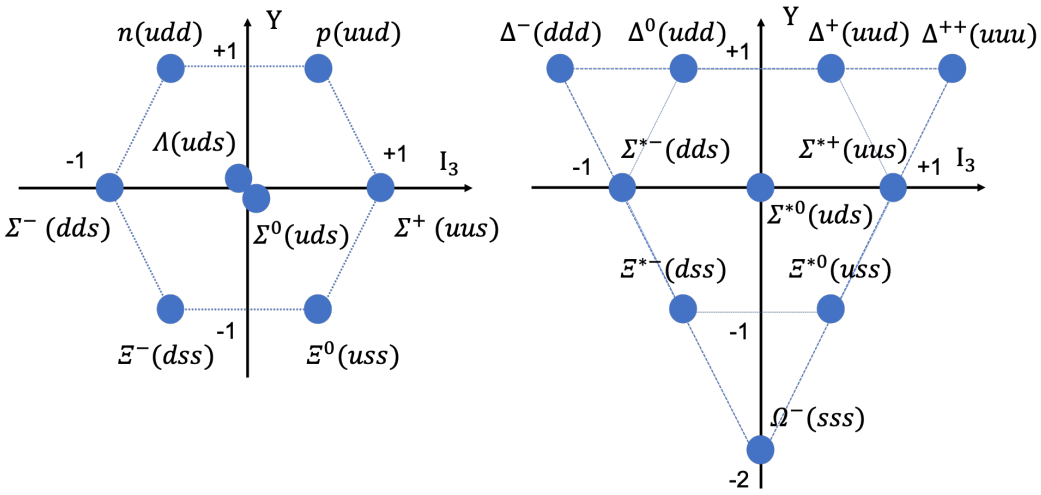

Fig. 1.3: (left) Baryon ($J = \frac{1}{2}$) in SU(3) (right) Baryon ($J = \frac{3}{2}$) in SU(3)

1.2.2 Exotic hadron

Since the quark model was established, few hadrons with structures other than baryons and mesons had been discovered. However, since the beginning of the 21st century, a number of exotic hadrons have been reported that cannot be explained by conventional hadron image. Exotic hadrons are called tetraquarks ($qq\overline{qq}$), pentaquarks ($qqqq\overline{q}$), and hexaquarks ($qqqqqq$), and so on, depending on the number of quarks, respectively.

The first exotic hadron observed was $X(3872)$[8], which consists of four quark configurations, reported by the KEK/Belle experiment in 2003. Starting from this report, peak structures have been observed in the invariant mass spectrum in the high energy region, such as $Y(4260)$[9], discovered by ISR (initial state radiation) searches and $P_c(4380)$ and $P_c(4450)$[10] observed by the LHCb group in 2015. However, the inner structure of all the exotic hadrons are not yet clarified. The nature of exotic hadrons is closely related to various properties of QCD, and it is expected that understanding what kind of quark structure is allowed in exotic hadrons will provide important information for the color confinement problem.

1.3 Dibaryon

One kind of the exotic hadrons, a composite particle consisting of six quarks is called a dibaryon, and especially a dibaryon containing multiple s quarks is called multi-strange dibaryon. As shown in the Fig.1.4, there are two possible states of the dibaryon: (i) multi-quark state, in which six quarks are compactly assembled, and (ii) baryon molecular state, in which two baryons are bound together. The multi-strange dibaryon has yet to be discovered, even though its existence has not been ruled

out by QCD. In either state (i) or (ii), If the dibaryon can be experimentally confirmed, it will be a new kind of hadron that does not correspond to the known quark model and will lead to further understanding of QCD.

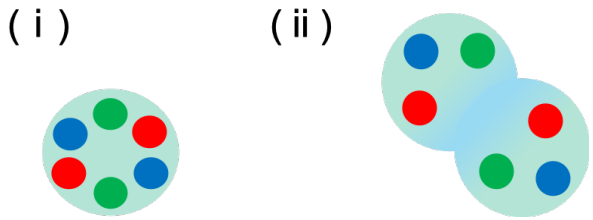

Fig. 1.4: Assumed dibaryon states (red, green, and blue circles represent quarks, respectively.)

1.3.1 Baryon-baryon interaction in flavor SU(3)

The baryon-baryon interaction is an essential information for considering the existence of dibaryon, and has been studied both theoretically and experimentally. By understanding the baryon-baryon interaction in detail, we can learn the knowledge of whether there is enough attraction to form a bound state between the two baryons.

Theoretically, it has recently been calculated using lattice QCD, which is a first-principles QCD calculation. The latest lattice QCD calculations by the HAL QCD group have successfully reproduced the nuclear forces in agreement with nucleon-nucleon scattering data[11], which was previously difficult to achieve. The group has also calculated the hyperon-nucleon and hyperon-hyperon interactions with the realistic quark masses, and the results indicate the possible existence of several multi-strange dibaryons.

Experimentally, two-particle correlation measurements using high energy hadron collisions are major method. The two-particle correlation function $C(k^*)$ is expressed with the distribution function of the particle emission source and the two particle wave function ψ, as in Eq.1.8, where r^* is the two-particle relative distance and k^* is the two-particle relative momentum.

$$C(k^*) = \int S(r^*)|\psi(k^*, r^*)| \tag{1.8}$$

The measurement of Sirius' angular diameter is a famous example of extracting the emission source size from this relation using two-photon correlations and two-particle wave function[12]. The $C(k^*)$ can be obtained by dividing the number of pairs N_{same} that satisfy a certain k^* for particles produced in the same collision by the number of pairs N_{mixed} that satisfy a certain k^* for particles produced in different collisions, as in Eq.1.9 [13]. In this equation, $\zeta(k^*)$ is the correction factor for the experimental effect.

$$C(k^*) = \zeta(k^*)\frac{N_{same}(k^*)}{N_{mixed}(k^*)} \tag{1.9}$$

The measured $C(k^*)$ can be mapped to the type of interaction between the two particles corresponding to its value (Fig.1.5). When the $C(k^*)$ value is higher than 1, there is an attractive force between the two particles, and when it is less than 1, there is a repulsive force. Furthermore, the two-particle wave function ψ can be determined by using a dynamical emission source, which modeled on various hadron measurements. Thus, it is possible to derive the two-particle potential experimentally and compare it with that calculated theoretically.

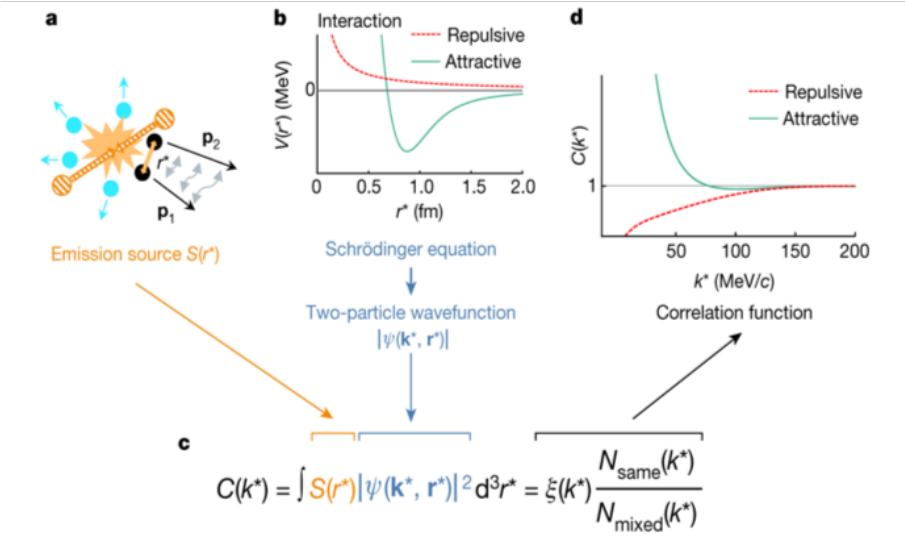

Fig. 1.5: Mapping of two-particle correlation functions to interactions[13] **a** : A baryon pair produced from a source in hadronic collisions interacting with each other **b** : An example of the potential between a pair **c** : Definition of the correlation function **d** : Relationship between potential and correlation function of a pair

1.3.2 H dibaryon

It is a multi-strange dibaryon consisting of quark configurations $uuddss$, which was first predicted by Robert Jaffe in 1977[14]. Since the Pauli blocking does not work, it is a leading candidate for dibaryon and has been searched for many years. Based on its quark configuration, it is expected to be a molecular state of $\Lambda\Lambda$ or $p\Xi$, as shown in (ii) of Fig.1.4. In the $\Lambda\Lambda$ bound state search performed by the LHC-ALICE experiment in 2016, no evidence for its existence was obtained[15]. On the other hand, the possibility of the existence of $\Lambda\Lambda$ bound state was discussed based on the Λ-Λ femtoscopic results. Fig.1.6 shows the exclusion plot of the Λ-Λ scattering parameters obtained from pp and p-Pb collisions data in the LHC-ALICE experiment[16]. The coloring indicates the difference of confidence level when certain parameters are excluded. In this figure, f_0 is the scattering length, and d_0 is the effective length. According to the standard sign convention in femtoscopy, a positive f_0 corresponds to an attractive interaction, while a negative f_0 corresponds to a repulsive potential ($d_0 > |f_0|/2$) or a bound state ($d_0 < |f_0|/2$). Based on this interpretation, there still remains the possibility that $\Lambda\Lambda$ exists as a bound state, since the negative f_0 and $d_0 < 4$ slight regions are not excluded.

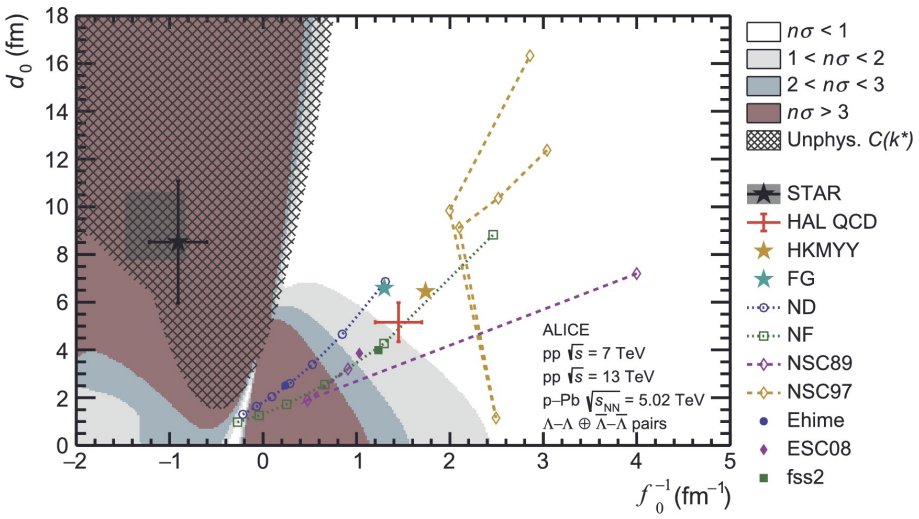

Fig. 1.6: Exclusion area in the Λ-Λ scattering parameters [16]

In 2020, the correlation function measurements of Λ-Λ [17] and p-Ξ[18]by the same experiment are in good agreement with the HAL QCD results[13]. The upper plot of the Fig.1.7 shows the measurement of the p-Ξ correlation function using the ALICE experiment pp collision data. The black dots represent the observed data, and the green line represents the Coulomb force. This result shows that there is an attraction between proton and Ξ that exceeds the Coulomb force. On the other hand, the pink line is a prediction that adds the effects of the Coulomb force and the baryon force calculated by lattice QCD, and it agrees well with the data.

Most importantly, the HAL QCD group has suggested the existence of the H-dibaryon as a resonant state of $\Lambda\Lambda$ and $p\Xi$ from the results of the lattice QCD calculations[19].

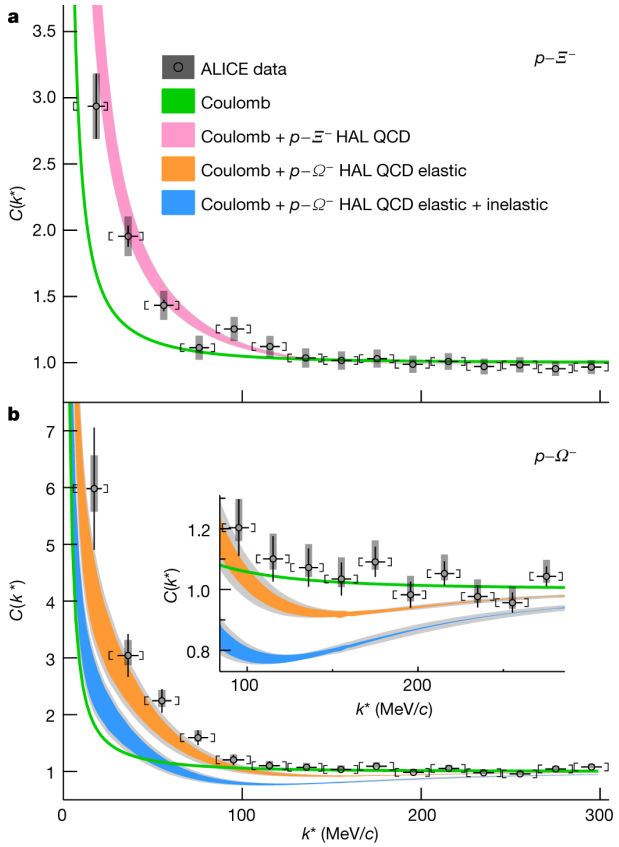

Fig. 1.7: p-Ξ and p-Ω correlation fuction [13]

1.3.3 $N\Omega$ dibaryon

It is a multi-strange dibaryon consisting of quark configurations $uudsss/uddsss$, and is also a leading candidate for dibaryons because the Pauli blocking does not work. The p-Ω correlation function measurement was performed in 2020 by the LHC-ALICE experiment[13]. The bottom plot of the Fig.1.7 shows the measurement of the p-Ω correlation function using the ALICE experiment pp collision data. The black dots represent the observed data, and the green line represents the Coulomb force. This result shows that there is an attraction between proton and Ω that exceeds the Coulomb force. The orange line is a prediction that adds the effects of the Coulomb force and the baryon force calculated by lattice QCD, and the blue line is the result of adding the effects of inelastic to the prediction of the orange line. The data are roughly consistent with the lattice QCD calculations, although there are still some uncertainties due to insufficient statistics and non-

consideration of strangeness-rearrangement caused by not measuring Λ-Ξ correlation function. The HAL QCD group suggest that the $N\Omega$ dibaryon exist a quasi-bound state[20]. Fig.1.8 shows the calculated binding energy B of p-Ω^- and n-Ω^- and the root mean square distance $\sqrt{\langle r \rangle^2}$. This results indicate that the binding energy of p-Ω^- is $2.46 \pm 0.34\mathrm{MeV}$ and the binding energy of n-Ω^- is $1.54 \pm 0.30\mathrm{MeV}$.

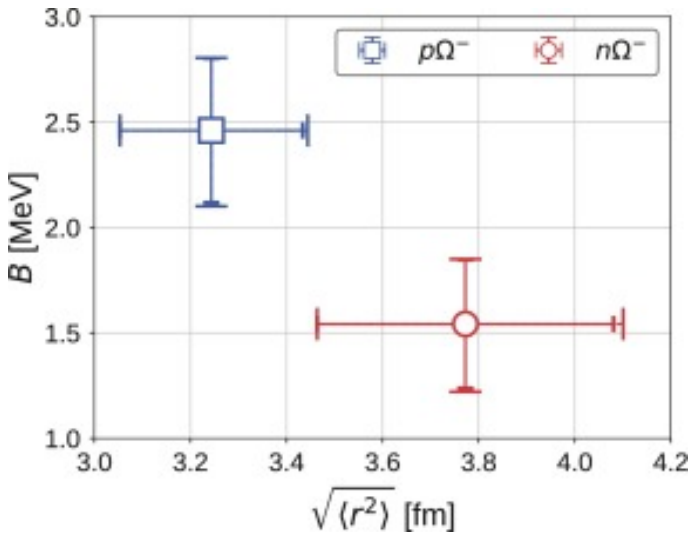

Fig. 1.8: Calculated p-Ω^- and n-Ω^- binding energy [20]

1.4 High energy hadron collisions

High energy hadron collisions began in the 1980s and are now being conducted at the Large Hadron Collider (LHC, European Organization for Nuclear Research) and the Relativistic Heavy ion Collider (RHIC, Brookhaven National Laboratory). The high temperature, high density state created by accelerating and colliding hadrons to near the speed of light can even produce particles with many strangeness that cannot exist in the normal state.

In order to experimentally produce multi-strangeness dibaryons, for example, hyperons scattering experiments are effective. However, such an experiment is technically difficult because hyperons have short lifetimes and are too unstable to be used as a beam. Hence, High energy hadron collisions is the only experiment for the dibaryon search now.

In proton-proton (pp) collisions, the strangeness enhancement is observed along with the increase of particle multiplicity, and the values at high multiplicity events reach similar values to those observed in Pb-Pb collisions (Fig.1.9). Furthermore, pp and proton-Pb (p-Pb) collisions have better hyperon purity than heavy ion collisions. In fact, at the LHC, we measured the correlations of Λ-Λ, p-Ξ, and p-Ω. Therefore, high-energy hadron collisions, especially high-multiplicity pp and p-Pb

collisions, are suitable for multi-strange dibaryon searches.

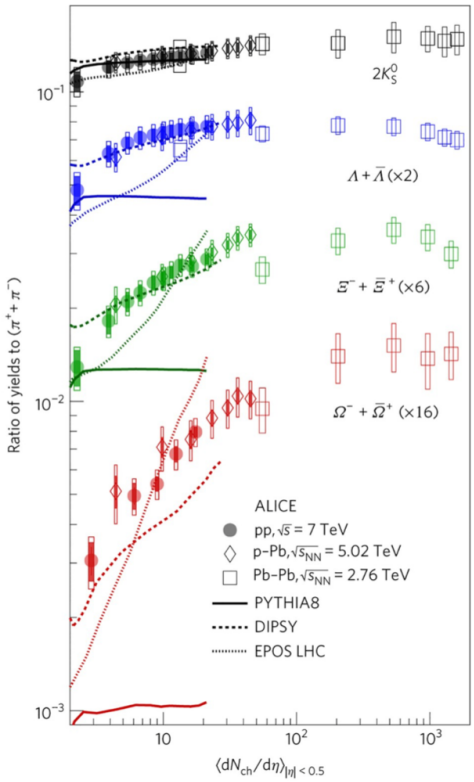

Fig. 1.9: Comparison of hyperon yield enhancement as a function of particle multiplicity in pp, p-Pb, and Pb-Pb collisions [21]

1.5 Dibaryon yields order estimation using statistical hadronization model

We used statistical hadronization model to estimate the yield of H and $N\Omega$ dibaryons in pp and p-Pb collisions, which have a better signal-to-noise ratio than Pb-Pb collisions. The statistical hadronization model is one of the models describing the hadronization. It is a thermal equilibrium model using a small number of parameters: temperature T_{ch}, volume V, and chemical potential μ when the hadron composition ratio is fixed in the reaction region. Fig.1.10 shows the results of the hadron yield observed in the ALICE experiment, where the red dots represent the observed data. The blue dotted line represents the yield calculated by the statistical hadronization model, and the solid blue line is the final yield calculation including decay production. This figure shows that the observed data agrees well with the values of the statistical hadronization model. Furthermore, the hadron yield does not depend on the type of hadron (baryon, meson, hyperon, deuteron, ^3He, etc.),

but only on its mass. Using this results, the yield in the presence of dibaryons is estimated using the assumed dibaryon masses and the total event number of pp and p-Pb collisions, as summarized in the Tab.1.1. This order calculations indicate that sufficient yields in H and $N\Omega$ dibaryon are expected in pp and p-Pb collision data.

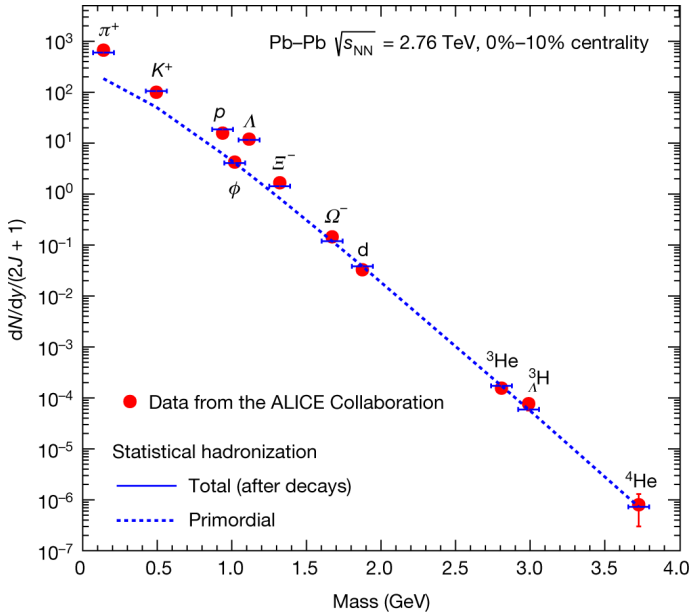

Fig. 1.10: Mass dependence of hyperon yields compared with predictios of the statistical hadronization model [22]

Search dibaryon	pp collision (High multiplicity)	p-Pb collision (Minimum bias)
H dibaryon	$\approx 10^{5-6}$	$\approx 10^{4-5}$
$N\Omega$ dibaryon	$\approx 10^{3-5}$	$\approx 10^{2-4}$

Tab. 1.1: Order estimation of dibaryon yields

1.6 Purpose of this study

Using the pp and p-Pb collision data measured by the LHC-ALICE experiment, we searched for H and $N\Omega$ dibaryons, whose existence is suggested by lattice QCD calculations. The purpose of this search is to contribute to the quark model by suggesting a new hadron form and to determine the binding energies of Λ-Λ and p-Ξ, and N-Ω system, which are additional information for understanding of the baryon interactions in the flavor SU(3) space.

2 Experimental setup

2.1 Large Hadron Collider (LHC)

LHC, built by European Organization for Nuclear Research (CERN), is the world's largest and most powerful particle accelerator (Fig.2.1). This accelerator is located about 100 meters underground on the Franco-Swiss border near Geneva, Switzerland. It consists of two LHC rings with a circumference of 27 km and a multi-stage accelerator (PS-SPS-LHC) [24]. Each accelerator accelerates the particle beam to a higher energy and injects it into the next accelerator. At the next accelerator, the particle beam is accelerated to higher energy. This process is repeated until the particle beam reaches its highest energy in the last ring, the LHC[25]. After a long shutdown for beam energy and beam luminosity enhancement of the LHC, the operation was restarted in 2015 and pp collisions were performed until 2018. In addition, Pb-Pb and p-Pb collisions were performed in 2015 and 2018, and 2016, respectively.

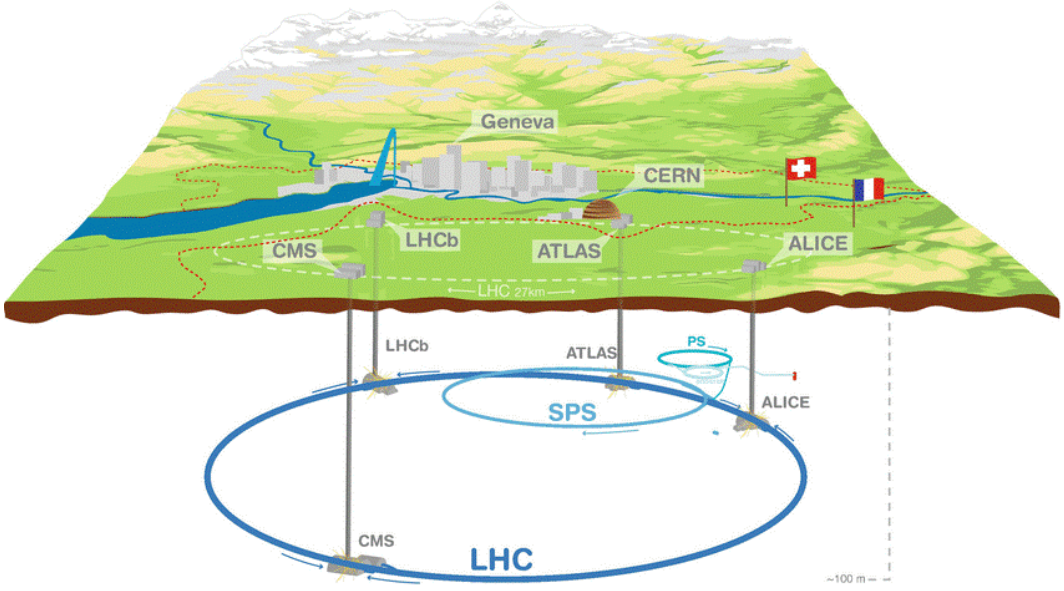

Fig. 2.1: The CERN accelerator complex [30]

2.2 A Large Ion Collider Experiment (ALICE)

ALICE is only experiment that optimized to heavy-ion physics at the LHC. The purpose is to reveal the physics of strongly interacting matter at extreme energy densities, where a phase of matter called Quark-Gluon Plasma(QGP) forms [26]. The ALICE detector (Fig.2.2) – 26m long, 16m high, and 16m wide – is capable of measuring the various particles produced in the experiments over a wide range of momentum [27]. It can be divided into three major parts (a) Central barrel, (b) Global detectors, and (c) Muon spectrometer. In the following section, I will focus especially on (a) and (b), which are involved in this analysis.

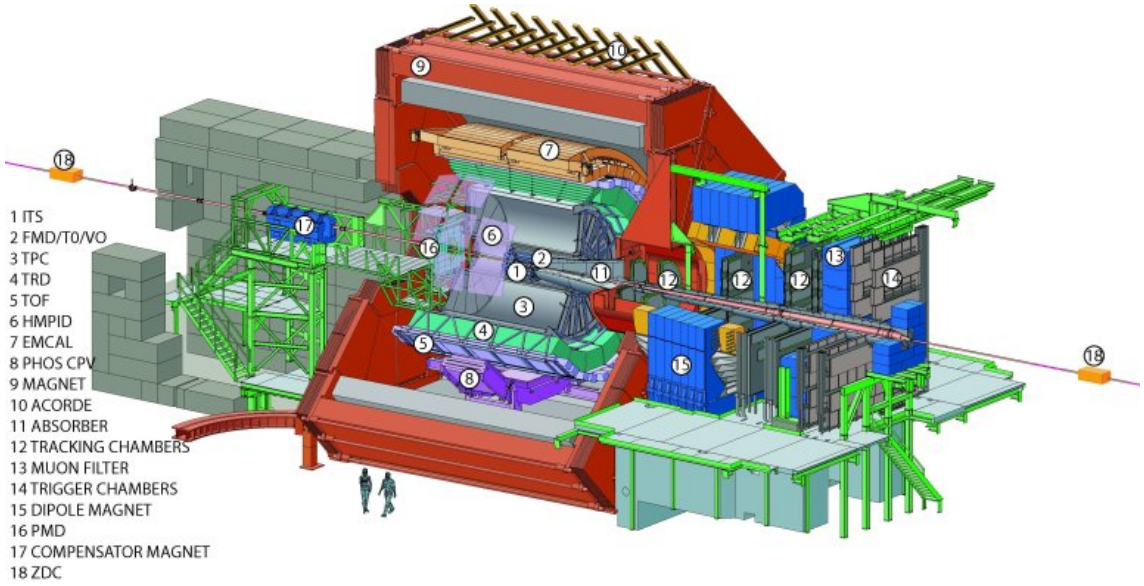

Fig. 2.2: A general view of the ALICE detector [30]

2.2.1 Central barrel

The central barrel consists mainly of Inner Tracking System (ITS), Time Projection Chamber (TPC), and Time of Flight (TOF), and is stored in a magnet with a magnetic field (0.5T). The generated charged particles at the collision points are affected by Lorentz force and are bent in their path. The central barrel reconstructs the particle tracks and measures the curvature for the momentum of the charged particles.

Inner Tracking Sytem (ITS)

The ITS (Fig.2.3) is the most central detector surrounding the collision points and consisted of six cylindrical layers with two layers each of : Silicon Pixel Detectors (SPD), Silicon Drift Detectors (SDD), and Silicon Strip Detectors (SSD) [31]. The main purpose of the ITS is to measure the points of charged particles passed through and collision points. By comparing with the TPC track information, it can contribute to the track reconstruction. The important rules of the ITS is as follows[32].

- Determination the collision points (primary vertices) with a resolution better than 100 micrometer
- Reconstruction the hyperon's decay points (secondary vertices)
- Identification the low-momentum particles
- Improvement the momentum and angle resolution for particles reconstructed by the TPC

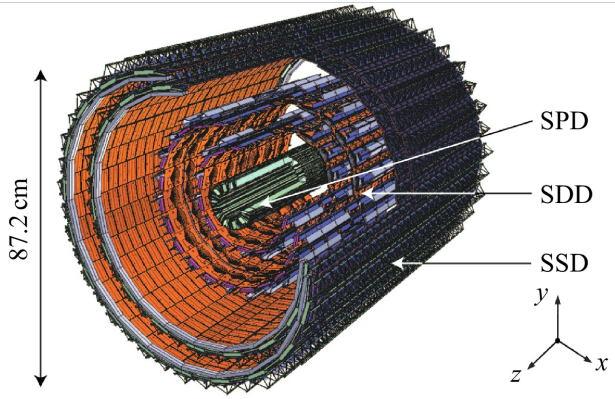

Fig. 2.3: An elevation view of the ITS [33]

Time Projection Chamber (TPC)

TPC (Fig.2.4) is located outside of the ITS and is the main device, in the central barrel, for tracking of charged particles and particle identification. The inner diameter is 85 cm, the outer diameter is about 247 cm, and the beam axial length is 500 cm, covering the region where $|\eta| < 0.9$. It is filled with Ne-CO2-N2 gas mixture. Charged particles traversing the TPC volume ionize the gas along their path, liberating electrons. The electrons are drifted towards the readout chamber by a uniform electric field (400 V/cm), and the three-dimensional track of the charged particles is

reconstructed from the position and time information of the electrons. At the same time, the readout system provides a energy loss, which is used for charged particle identification [35].

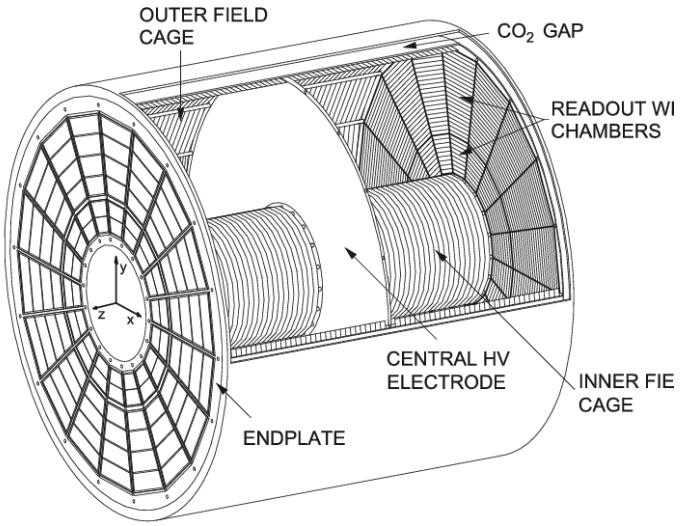

Fig. 2.4: A general view of the TPC [36]

Time of Flight (TOF)

TOF measures the flight time of each charged particle from the collision points to the point of arrival, so that one can identify charged particles. The ALICE TOF detector (Fig.2.5) is located at about 3.7 m from the collision points and is consisted of 1593 Multigap Resistive Plate Chambers (MRPCs) strip detector. The average time resolution was measured to be better than 50 ps. It is possible to identify pions and K mesons with momentum below 2.5 GeV/c and protons with momentum below 4 GeV/c by comparing with the TPC track information[37].

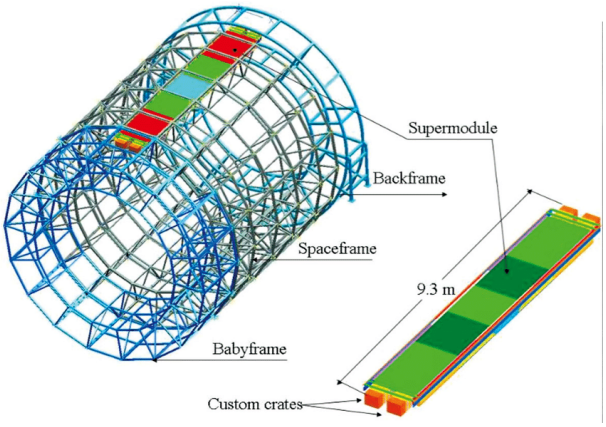

Fig. 2.5: Super Module of TOF [38]

2.2.2 Global detector

In high-energy heavy-ion collisions, nuclei may collide with each other in central or peripheral collisions. In order to classify these collisions, various global detectors (Fig.2.6)have been installed in the ALICE detector. The global detector consists of Zero Degree Calorimeter (ZDC), T0 detector, and V0 detector.

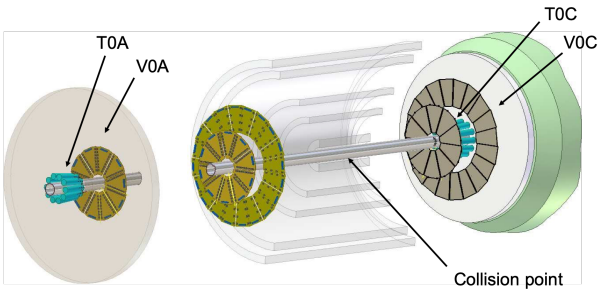

Fig. 2.6: Schematic of the placement of T0 and V0 detector [41]

Zero Degree Calorimeter (ZDC)

The ZDC is made by two identical sets of calorimeters located on both sides relative to the collision point, 112.5 meters away from it. Each set of detectors consists of 2 hadronic spaghetti calorimeters (Fig.2.7), neutron (ZN) and a proton (ZP) calorimeter. By the detection of Cherenkov light produced by the charged particles of the shower in the fibers, we can measure the energy of the spectator nucleons and determine the overlap region of nucleon-nucleon collisions. In Pb-Pb

collisions, ZDC provides the centrality of the collisions, event characterization, and minimum bias event selection[39].

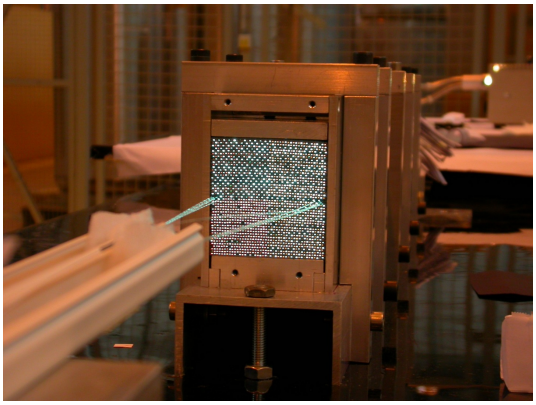

Fig. 2.7: Quarts-fiber spaghetti calorimeters [40]

T0 detector

The T0 detector consists of two Cherenkov counters (T0C and T0A) located at distances of about 72.7 cm and 375 cm from the collision point. T0C covers the region where $3.28 < |\eta| < 2.97$ and T0A covers the region where $4.61 < |\eta| < 4.92$. T0C and T0A has 12 cylindrical counters equipped with a quartz radiator and a photomultiplier tube, and T0 detector can measure the collision time with high precision (< 25 ps). This measurement is used to determine the position of the collision point along the beam axis (with precision of $\pm$ 1.5 cm) and the start time (T0) of the TOF[41].

V0 detector

The V0 detector consists of two scintillation detectors (V0A and V0C) located at distances of about 320 cm and 90 cm from the collision point. The V0A and V0C cover the pseudo-rapidity range $2.8 < |\eta| < 5.1$, $-3.7 < |\eta| < -1.7$, respectively. Based on the arrival time of the particles, V0 detector rejects the fake events generated by beam-gas interaction. In addition, The minimum bias trigger is determined when at least one hit is detected simultaneously in V0A and V0C[41].

3 Data analysis

3.1 Analyzed data and event selection

The data used for this study are pp collisions at $\sqrt{s} = 13$ TeV taken by the ALICE experiment in 2016-2018 and p-Pb collisions at $\sqrt{s_{NN}} = 5.02$ TeV taken in 2016. The minimum bias events (MB) and the high multiplicity events (HM) were selected as the collision types for p-Pb and pp collisions, respectively. An event that detects at least one signal in both V0A and V0C is MB, and an event where the particle multiplicity exceeds the threshold in the V0 and SPD detector is HM.

In addition, the quality of our analysis was improved by considering the following three points.

1. The removal of multiple collision events (Pile-up rejection)
2. The quality of the collision point
3. The location of the collision point

For point 1, the pileup events was rejected in which multiple primary vertexes are reconstructed by SPD. Next, for point 2, we confirmed whether SPD was involved in the reconstruction of the collision points, whether the beam axial resolution of the collision points reconstructed by SPD was less than 0.25 cm, and whether the difference between the beam axial resolution of the collision points reconstructed by TPC and SPD was less than 0.5 cm. Finally, for point 3, we confirmed if the difference in the beam axis between the reconstructed collision point and the standard collision point was less than 10 cm. The number of events in pp and p-Pb collisions after these event selection is summarized in the Tab.3.1.

Collision system	number of event
pp collisions (V0 HMtrigger)	1.3×10^9
pp collisions (SPD HMtrigger)	4.7×10^8
p-Pb collisions (MB)	6.0×10^8

Tab. 3.1: Event number in each trigger

3.2 Particle identification (PID)

Charged pions, charged kaons, and protons, which are decay particles of hyperons, taken from selected charged particle samples by particle identification (PID) using TPC and TOF. In this section, the principle of PID for TPC and TOF are explained.

3.2.1 PID using TPC information

Scattering with electrons in atoms and molecules is the dominant reaction when charged particles pass through a material. In this process, the electron gains energy from the charged particle, and if that energy is sufficiently higher than the electron's binding energy, the electron is released from the atom or molecule. The energy loss of the charged particles is expressed by Eq. 3.1.

$$-\frac{dE}{dx} = nZz^2\frac{4\pi\alpha^2(\hbar c)^2}{m_e c^2\beta^2}\left(\ln\frac{2m_e c^2\beta^2\gamma^2}{I} - \beta^2\right) \tag{3.1}$$

In Eq 3.1, -dE is the energy loss while passing a distance dx, n is the density of atoms in the material, Ze is the charge of the material atom, m_e is the mass of the electron, and βc and ze are the velocity and particle's charge. In addition, I is a parameter called the average excitation potential of material atoms. An important feature of this equation is that the energy loss per unit length $-dE/dx$ is determined only by the charge and velocity of the particle, regardless of the type of particle. Hence the behavior of the energy loss corresponding to the momentum in a material depends on the particle's mass. This property can be used to identify the charged particle.

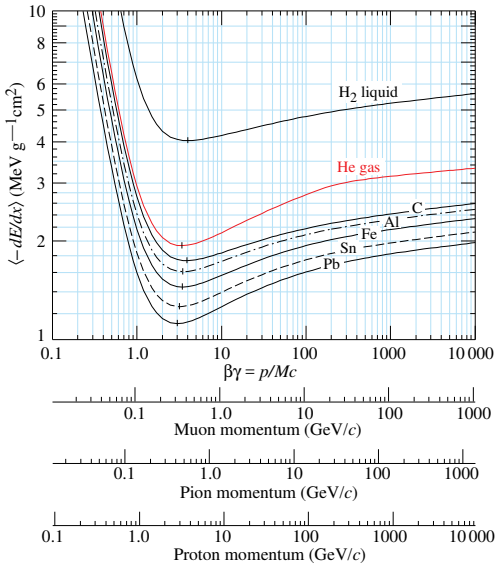

Fig. 3.1: Energy loss of charged particles in matters [42]

When a charged particle passes through the ALICE-TPC, it drops its energy into the gas and ionized electrons are generated corresponding to its amount. The ionized electrons drift to reach the readout, and the amount of signal is proportional to the energy loss. Thus the energy loss dE/dx for a track can be determined. In the ALICE experiment, equation 3.1 is parameterized as in Eq.3.2 [43].

$$\frac{dE}{dx} = \frac{P_1}{\beta^{P_4}} \left(P_2 - \beta^{P_4} - \ln \left(P_3 + \frac{1}{(\beta\gamma)^{P_5}} \right) \right) \tag{3.2}$$

P_1 ~ P_5 are parameters determined by fitting with experimental data, and take different values for each particle. Fig.3.2 shows the relationship between the dE/dx resolution and charged particle's total momentum in p-Pb collision at $\sqrt{s_{NN}} = 5.02$ TeV. The energy resolution reaches about 5% at the maximum number of TPC clusters 159.

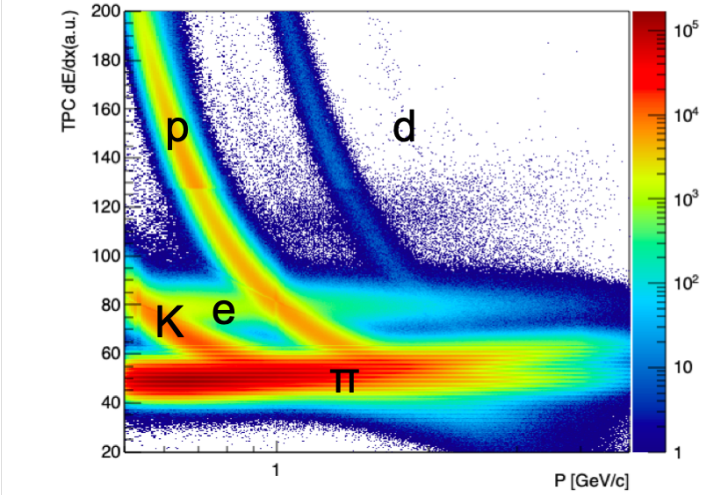

Fig. 3.2: Energy loss distribution measured by TPC

3.2.2 PID using TOF information

The TOF PID is performed by measuring the time between the collision time measured by the T0 detector and the arrival of the particle at the TOF. It requires that the difference between the measured time of flight and the value expected from the particle's track, mass, and momentum be less than a certain threshold, as shown in Eq.3.3 [44].

$$n_{\sigma,\mathrm{TOF}} \equiv \frac{(t_{\mathrm{TOF}} - t_{ev}) - t_{exp}(m,p,L)}{\sigma_{tot}} \tag{3.3}$$

In this equation, t_{TOF} is the arrival time measured by the TOF, t_{ev} is the time of the collision event, and t_{exp} is the time of flight expected to be required for a particle of mass m, momentum

p, and track length L to reach the TOF from the collision point. In addition, σ_{tot} represents the total resolution determined by the TOF detector's resolution, the uncertainty of the collision event time, and the uncertainty of the track reconstruction. Fig.3.3 shows the velocity β of the particle obtained from the TOF and TPC information plotted as a function of momentum in p-Pb collision at $\sqrt{s_{NN}} = 5.02$ TeV. This figure shows the separation of electrons and π, K mesons, and protons at mid-transverse momenta.

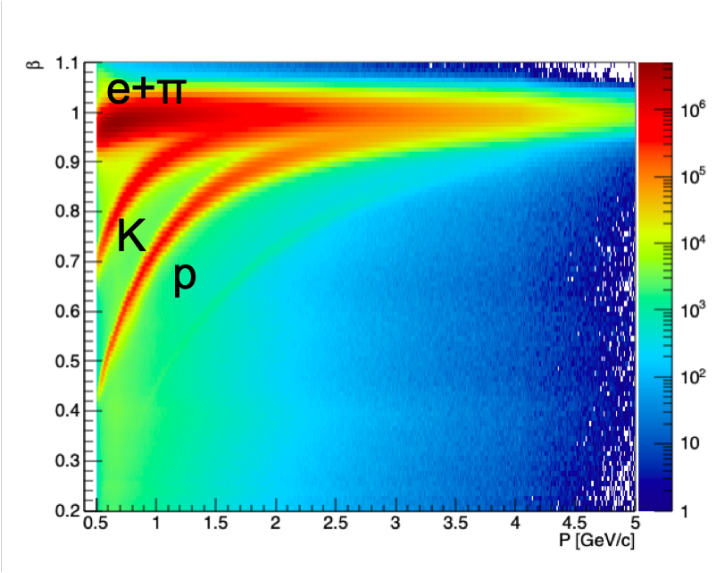

Fig. 3.3: Velocity β distribution measured by TOF

3.3 Invariant mass

PID by TPC and TOF is effective only for electrons and charged hadrons with long lifetimes, such as protons. Neutral hadrons and short-lived particles cannot be observed directly. However, if these particles eventually decay into stable charged particles, they can be observed indirectly by reconstructing invariant mass distribution of these charged particles. In this study, invariant mass distributions were used to reconstruct hyperons such as Λ and Ξ to search for dibaryons.

We consider a particleX with four-momentum (E,$\boldsymbol{p}$) decays into particle1 and particle2. When the four-momenta of charged particles1 and particle2 are $p1$ = ($E1$, $\boldsymbol{p1}$) and $p2$ = ($E2$, $\boldsymbol{p2}$), respectively, their invariant masses are as follows.

$$M_X \equiv \sqrt{(E_1 + E_2)^2 - (\mathbf{p_1} + \mathbf{p_2})^2} \tag{3.4}$$

Therefore, the invariant mass is calculated for these pairs of charged particles1,2 and create mass distribution, a peak appears at the particleX's mass m. Since background appears in the invariant

mass distribution due to uncorrelated charged particle combinations or misidentified charged particles, it is necessary to show that the peak signal is significant compared to the background in the real data.

3.4 Candidate selection

In this study, the selection criteria have been adopted used in [17] [18] to select proton, Λ, and Ξ. The selection criteria for each are summarized in this section.

3.4.1 Proton candidate selection

The selection criteria for the proton candidates are summarized in Tab.3.2. The pseudorapidity range is taken into account from the acceptance of the central barrel. For the transverse momentum, a low transverse momentum cutoff is applied to minimize the number of protons originating from the interaction between the primary particle and the detector. In addition, at high transverse momentum, the separation power of TPC and TOF PID decreases and the purity drops below 80 %, thus a cutoff is applied to increase the purity. The selection using TPC clusters is effective in ensuring track quality and good pT resolution at large momentum, and in removing false tracks from the sample. The distance of closest approach (DCA) is the closest distance from the track to the primary vertex and is selected using both the DCA perpendicular to the beam axis (DCAxy) and the DCA parallel to the beam axis (DCAz). This selection is effective for distinguishing protons coming from primary vertex. For proton PID, both TPC and TOF detectors are employed. At momentum below $p < 0.75$ GeV/c, only PID selection from the TPC is applied. On the other hand, both detectors are used at larger momentum because the TPC does not provide sufficient separation power. The TPC and TOF signals are combined as shown in Eq 3.5.

$$n_{\sigma,combined} \equiv \sqrt{(n_{\sigma,TPC})^2 + (n_{\sigma,TOF})^2} \tag{3.5}$$

In this equation, n_σ is the standard deviations of the measured value from the expected signal at a momentum.

Selection criterion	Value
Pseudorapidity	$\mid \eta \mid < 0.8$
Transverse momentum	$0.5 < p_T < 4.05$ GeV/c
TPC cluster	$n_{\mathrm{TPC}} > 80$
Crossed TPC pad rows	$n_{crossed} > 70$ (out of 159)
Findable TPC clusters	$n_{crossed}/n_{findable} > 0.83$
Tracks with shared TPC clusters	rejected
Distance of closest approach xy	$\mid \mathrm{DCA_{xy}} \mid < 0.1$ cm
Distance of closest approach z	$\mid \mathrm{DCA_{z}} \mid < 0.2$ cm
Particle identification	$\mid n_{\sigma}, \mathrm{TPC} \mid < 3$ for $p < 0.75$ GeV/c $n_{\sigma}, combined < 3$ for $p > 0.75$ GeV/c

Tab. 3.2: proton selection criteria

3.4.2 Λ candidate selection

Λ has the weak decay process : $\Lambda \longrightarrow p\pi^-$ ($\mathrm{BR} = 63.9\%, \mathrm{c}\tau = 7.3\mathrm{cm}$). The Λ produced at the collision point decays into two charged particles have different signs at a distance of several cm from the collision point. These charged particles are forced in opposite directions by the magnetic field, and their tracks are shown in Fig.3.4. The process of decaying from an uncharged particle such as Λ to two charged particles is called V0 decay because it has a geometric feature the detected shape of the track looks like the letter V. Since Λ has no charge, it cannot be detected directly. However, we can reconstruct it by using the characteristic V0 decay.

The selection criteria for the Λ candidates are summarized in Tab.3.3. For proton and π, which are V0 daughter tracks, only TPC information is used for PID in order to obtain Λ candidates efficiently. In addition, to reject background from out-of-bunch multiple collisions at the outside of the SPD readout time, hit information in ITS (SPD or SDD) or TOF is required.

After the daughter track selection, all the positively charged daughter tracks with their negatively charged partners are combined. For the (p, π^-) pairs obtained in this way, V0 selection considering an appropriate topological cut to suppress the background is next required. The cut parameter is shown below.

Transverse radius of the decay vertex Since Λ is a neutral particle, the Λ decay vertex is expected to be far from the collision point. Therefore, we required lower and upper limits for the radius of the V0 decay vertex perpendicular to the beam, taking into account the lifetime of Λ.

DCA of the daughter tracks at the decay vertex The decay particles of Λ, proton are produced at the same decay vertex. Hence, it is necessary to select the distance between the two particle track that is close to each other.

Pointing angle α Pointing angle α is the opening angle between the Λ momentum vector and the vector from the primary vertex to the V0 decay point. Since the V0 particle is neutral and not

affected by magnetic fields, cosα (CPA) should be close to 1.

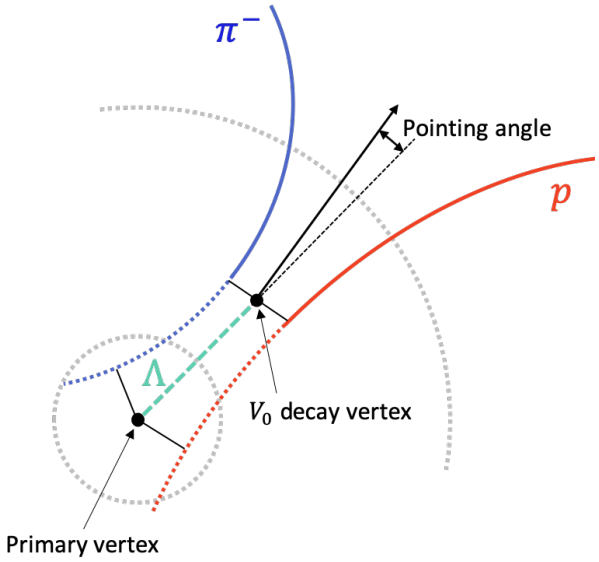

Fig. 3.4: Λ decay topology

In addition to these topological cuts, the $K0_s$ rejection also need to consider to increase the purity of Λ. This cut is required when a particle that is really π is misidentified as a proton by TPC PID. In this case, $K0_s$ with the decay process : $K0_s \longrightarrow \pi^+\pi^-$ is incorrectly identified as Λ. Therefore, if the error from PDG value of the $K0_s$ mass ($497.611 \pm 0.013\,\mathrm{MeV/c^2}$) is within about $20\,\mathrm{MeV/c^2}$ when the two particles (π^+, π^-) are reconstructed, such a pair will be rejected.

Finally, two particles satisfying these criteria and whose reconstructed mass is within $4\,\mathrm{MeV/c^2}$ from PDG value of the Λ mass ($1,115.683 \pm 0.006\,\mathrm{MeV/c^2}$) are considered Λ. Fig.3.5 shows the invariant mass distribution of Λ in pp and p-Pb collisions reconstructed by these Λ selections. In both collision systems, the Λ purity is more than 90%, which clearly confirms that Λ is produced.

Selection criterion	Value
Daughter track selection criteria	
Pseudorapidity	$\mid \eta \mid < 0.8$
TPC cluster	$n_{\mathrm{TPC}} > 70$
Distance of closest approach	$\mathrm{DCA} > 0.05$ cm
Particle identification	$\lvert n_{\sigma}, \mathrm{TPC} \rvert < 5$
Out-of-bunch pile-up removal	Hit in ITS SPD or SSD or TOF timing
V0 selection criteria	
Transverse momentum	$0.3 < p_T$ GeV/c
Λ decay vertex	$\lvert i_{vertex\Lambda} \rvert < 100$ cm, $i = x, y, z$
Transverse radius of the decay vertex r_{xy}	$0.2 < r_{xy} < 100$ cm
DCA of the daughter tracks at the decay vertex	$\mathrm{DCA}(\lvert \mathrm{p}, \pi \rvert) < 1.5$ cm
Pointing angle α	$\cos\alpha > 0.99$
K0 rejection	$0.48 < M_{\pi^+\pi^-} < 0.515$ GeV/c^2
Λ mass window	$\lvert M_{p,\pi} - M_{\Lambda,\mathrm{PDG}} \rvert < 4$ MeV/c^2

Tab. 3.3: Λ selection criteria

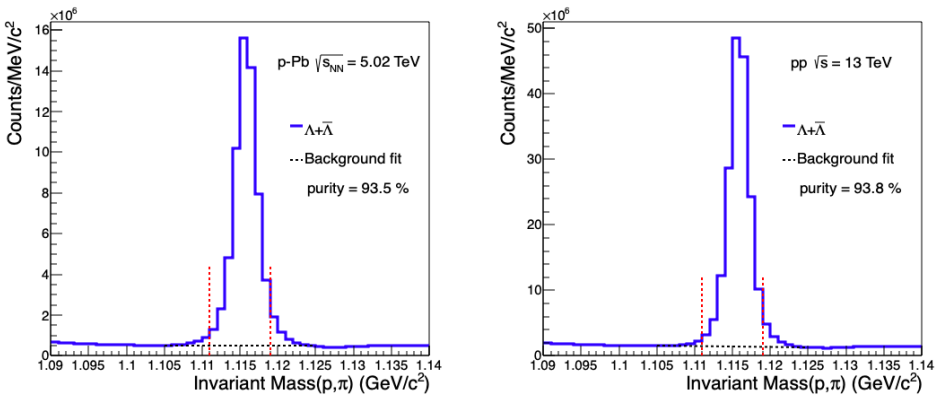

Fig. 3.5: Λ invariant mass

3.4.3 Ξ^- candidate selection

Ξ^- has the weak decay process : $\Xi^- \longrightarrow \Lambda\pi^-$ $(\mathrm{BR} = 99.9\%, c\tau = 4.9\mathrm{cm})$. The charged particle, Ξ^-, can be detected directly in principle. However, due to its short lifetime, it quickly decays into Λ and π and cannot be identified by itself. Since Λ further decays into two particles, Ξ^- need to reconstruct three tracks (p, π, π), and this decay process is called cascade decay (Fig.3.6). The cascade decay is reconstructed by matching a third track π (=bachelor track) to two tracks (p, π) of V0 decay particles. The selection criteria for the Ξ^- candidates are summarized in Tab.3.4.

First, we show the criteria for Ξ^- three daughter tracks. For proton and two π, which are Ξ^- daughter tracks, only TPC information is used for PID in order to obtain Ξ^- candidates efficiently. Furthermore, a lower limit was set for the value of DCA because it is necessary to remove tracks coming from the collision point.

Next, Ξ^- decay Λ requires V0 selection as in Tab.3.3, and also requires the rejection of V0 particles coming directly from the collision point. Hence, we set lower limits for the distance from the primary vertex to the each Λ decay tracks (= DCA of the Λ to the primary vertex) and transverse radius. In addition, since the Ξ^- yields is relatively few compared to other particles, we aim to secure a large number of Ξ^- decay Λ candidates by loosening the CPA and mass cut.

The final selection criteria are applied directly to the Ξ^- candidate. The distance of closest approach of the three daughters with respect to the Ξ^- decay vertex (=DCA of the daughter tracks at the Ξ^- decay vertex) is used as a quality criterion. Furthermore, by combining the momentum of the bachelor track and Λ and using the opening angle α between this and the vector pointing to the decay vertex from the primary vertex, we can distinguish false candidates due to combinatorial background.

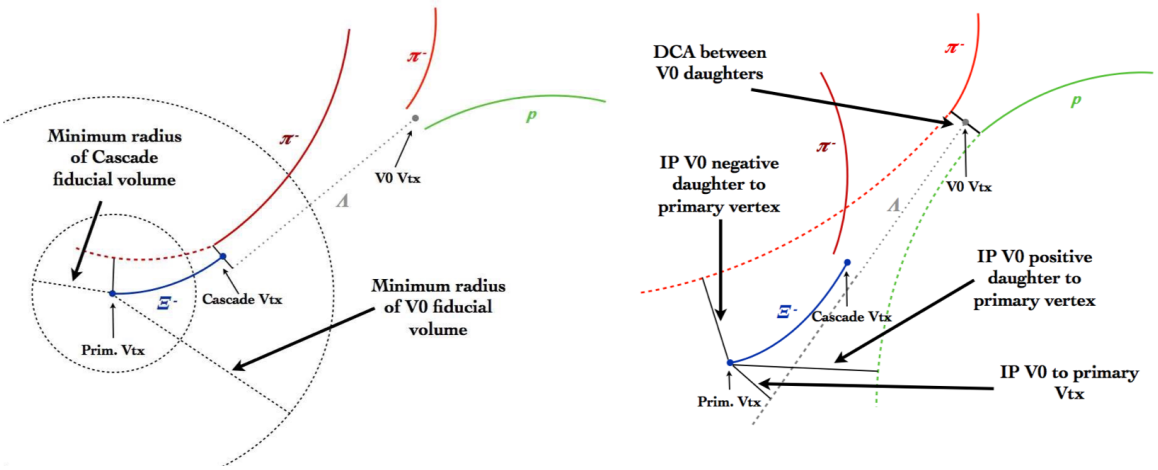

Fig. 3.6: Ξ^- decay topology

In addition to these Ξ^- topological cuts, the Ω rejection also need to consider to increase the purity of Ξ^-. This cut is required when a particle that is really π is misidentified as a K meson by TPC PID. In this case, Ω^- with the decay process $\Omega^- \longrightarrow \Lambda K^-$ is incorrectly identified as Ξ^-. Therefore, if the error from the PDG value of Ω^- mass ($1672.45 \pm 0.29\ \mathrm{MeV/c^2}$) is within about $5\ \mathrm{MeV/c^2}$ when the three particles (p, π, K) are reconstructed, such a track combination will be rejected.

Finally, three particles satisfying these criteria and whose reconstructed mass is within $5\ \mathrm{MeV/c^2}$ from PDG value of the Ξ^- mass ($1321.31 \pm 0.13\ \mathrm{MeV/c^2}$) are considered Ξ^-. Fig.3.7 shows the invariant mass distribution of Ξ^- in pp and p-Pb collisions reconstructed by these Ξ^- selections. In both collision systems, the Ξ^- purity is more than 90%, which clearly confirms that Ξ^- is produced.

Selection criterion	Value
Daughter track selection criteria	
Pseudorapidity	$\mid \eta \mid < 0.8$
TPC cluster	$n_{\mathrm{TPC}} > 70$
Transverse momentum	$0.3 < p_T$ GeV/c
Distance of closest approach	$\mathrm{DCA_{Bachelor}} > 0.05$ cm
Distance of closest approach	$\mathrm{DCA_{V0Daughters}} > 0.05$ cm
Particle identification	$\lvert n_\sigma, \mathrm{TPC} \rvert < 4$
Λ selection criteria	
Λ Pointing angle α	$\cos\alpha > 0.97$
Transverse radius of the Λ decay vertex r_{xy}	$1.4 < r_{xy} < 200$ cm
DCA of the daughter tracks at the Λ decay vertex	$\mathrm{DCA}(\lvert \mathrm{p}, \pi \rvert) < 1.5$ cm
DCA of the Λ to the primary vertex	$\mathrm{DCA} > 0.07$ cm
Λ mass window	$\lvert M_{p,\pi} - M_{\Lambda,\mathrm{PDG}} \rvert < 6\ \mathrm{MeV/c^2}$
Ξ^- selection criteria Ξ^- Pointing angle α	$\cos\alpha > 0.98$
Transverse radius of the Ξ^- decay vertex r_{xy}	$0.8 < r_{xy} <$200 cm
DCA of the daughter tracks at the Ξ^- decay vertex	$\mathrm{DCA}(\lvert \mathrm{p}, \pi, \pi \rvert) <$1.6 cm
Ω^- rejection	$1.667 < M_{p,K,\ \pi^-} < 1.677\ \mathrm{GeV/c^2}$
Ξ^- mass window	$\lvert M_{p,\pi,\pi} - M_{\Xi^-,\mathrm{PDG}} \rvert < 5\ \mathrm{MeV/c^2}$

Tab. 3.4: Ξ^- selection criteria

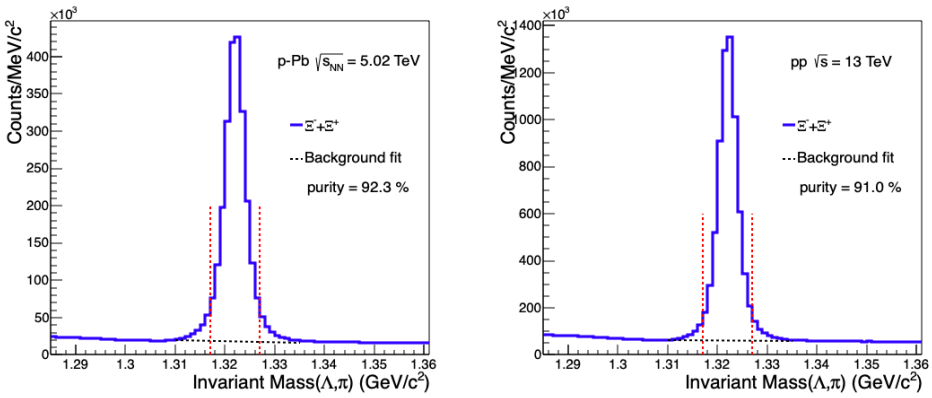

Fig. 3.7: Ξ^- invariant mass

3.5 Dibaryon mass resolution

There is no theoretical prediction for the diversion signal width. Therefore, it is necessary to determine the width of the signal and search for it. In this section, the dibaryon mass resolution was discussed based on the simulation to set the minimum signal width.

3.5.1 $\Lambda\Lambda$ mass resolution

We used the Monte-Carlo event generator EPOS-LHC[45] anchored LHC p-Pb collisions $\sqrt{s_{NN}} = 5.02$ TeV to determine the resolution. Fig.3.8 shows the results of a Gaussian fit on the difference distribution between the true $\Lambda\Lambda$ invariant mass with the H dibaryon signal region ($2.231 < \Lambda\Lambda < 2.26$ GeV/c^2) and the reconstructed invariant mass. From the value of standard deviation by this fit, we determined that $\Lambda\Lambda$ resolution is 0.9538 ± 0.0727 MeV/c^2.

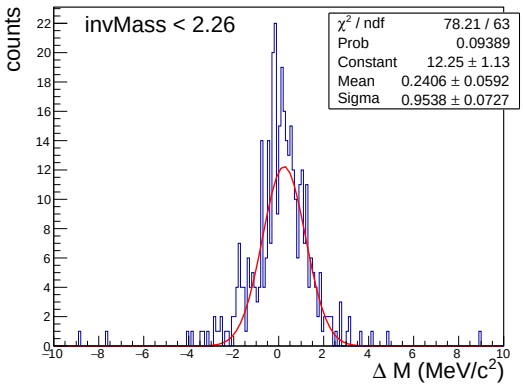

Fig. 3.8: $\Lambda\Lambda$ resolution

3.5.2 $p\Xi$ and $\Lambda\Xi$ mass resolution

In this time, we could not obtain sufficient statistics for $p\Xi$ and $\Lambda\Xi$ with the dibaryon signal region ($2.26 < p\Xi < 2.36$ GeV/c^2 and $2.437 < \Lambda\Xi < 2.61$ GeV/c^2), so we could not determine these resolution in the same way as for $\Lambda\Lambda$. However, since the pair p_T and the opening angle ϕ resolution affect the mass resolution, we discuss the results of p_T and ϕ resolution (p_T separation) for single Λ and single Λ to guess the approximately values of $p\Xi$ and $\Lambda\Xi$ resolution compared to $\Lambda\Lambda$.

p_T resolution

Figure 3.9 (left) shows the p_T dependence of p_T resolution for single Λ and Ξ. Although the p_T resolution tends to get worse with increasing p_T, the trend is almost similar for Λ and Ξ. Thus, the difference in the effect of the p_T resolution of Λ and Ξ on the mass resolution is almost no negligible.

ϕ resolution

Figure 3.9 (right) shows the p_T dependence of the ϕ resolution for single Λ and Ξ. In both cases, the ϕ resolution tends to improve with increasing p_T, but the resolution of single Λ is several times better than that of Ξ. Since the ϕ resolution of proton is expected to be better than that of Λ, the $p\Xi$ mass resolution is expected to be comparable to that of $\Lambda\Lambda$. Furthermore, the $\Lambda\Xi$ mass resolution is expected to be lower than $\Lambda\Lambda$ mass resolution due to the lower ϕ resolution.

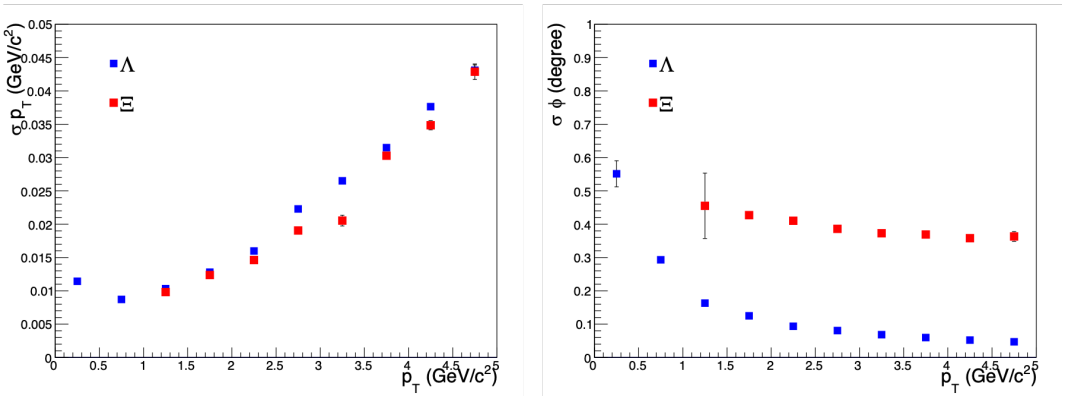

Fig. 3.9: (left) p_T resolution p_T dependence (right) ϕ resolution p_T dependence

4 Result and Discussion

4.1 Pair invariant mass distribution

The number of $\Lambda\Lambda$ ($\bar{\Lambda}\bar{\Lambda}$), $p\Xi^-$ ($\bar{p}\Xi^+$), and $\Lambda\Xi^-$ ($\bar{\Lambda}\Xi^+$) pairs in p-Pb and pp collisions by combining these decay particle candidate are shown in Tabs. 4.1, 4.2. In addition, the reconstructed $\Lambda\Lambda$ ($\bar{\Lambda}\bar{\Lambda}$), $p\Xi^-$ ($\bar{p}\Xi^+$), and $\Lambda\Xi^-$ ($\bar{\Lambda}\Xi^+$) invariant mass distributions near the signal region are shown in Figs. 4.1, 4.2, 4.3. These figures show that sufficiently clear dibaryon signala cannot be identified for background.

Pair	number
$\Lambda\Lambda$ ($\bar{\Lambda}\bar{\Lambda}$)	2.5×10^6
$p\Xi^-$ ($\bar{p}\Xi^+$)	8.7×10^5
$\Lambda\Xi^-$ ($\bar{\Lambda}\Xi^+$)	2.1×10^5

Tab. 4.1: Number of pairs in p-Pb collisions

Pair	number
$\Lambda\Lambda$ ($\bar{\Lambda}\bar{\Lambda}$)	2.6×10^7
$p\Xi^-$ ($\bar{p}\Xi^+$)	6.8×10^6
$\Lambda\Xi^-$ ($\bar{\Lambda}\Xi^+$)	2.0×10^6

Tab. 4.2: Number of pairs in pp collisions

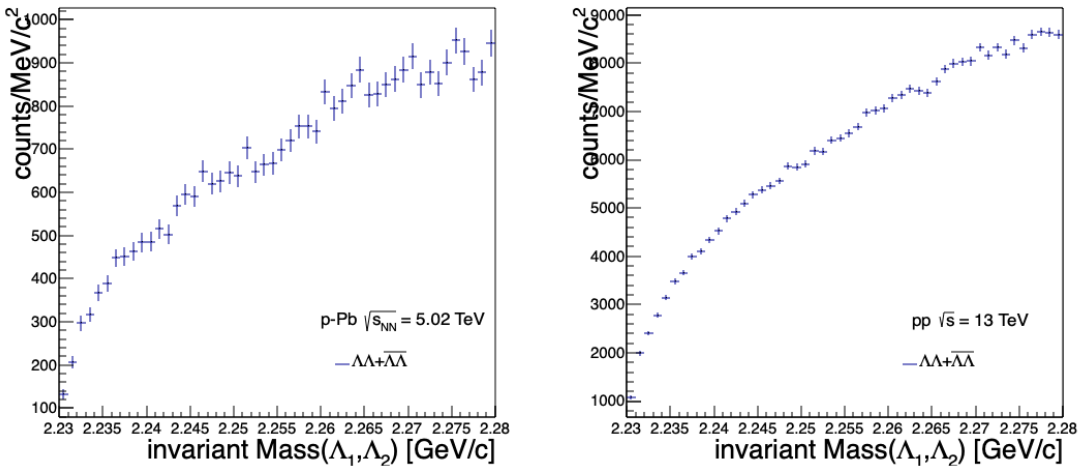

Fig. 4.1: $\Lambda\Lambda$ ($\bar{\Lambda}\bar{\Lambda}$) invariant mass distributions for p-Pb (left) and pp (right)

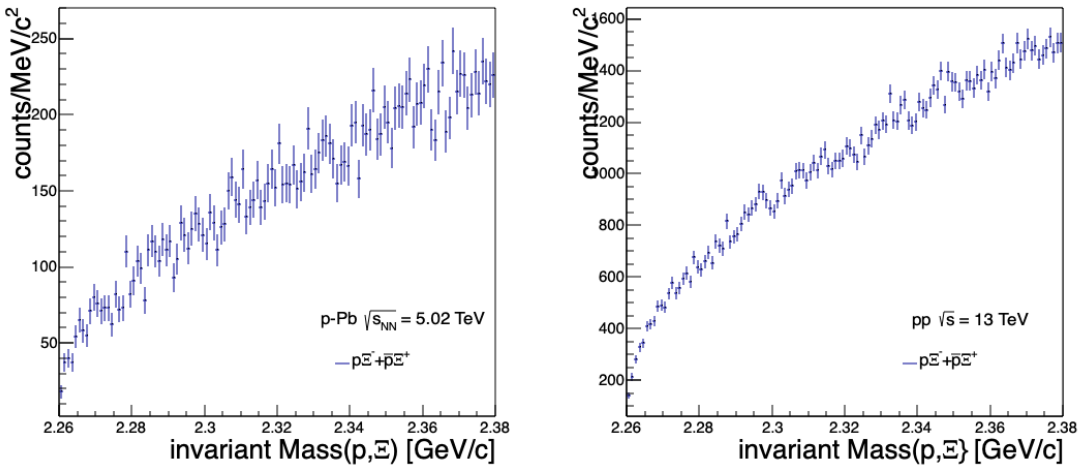

Fig. 4.2: $p\Xi^-$ ($\bar{p}\Xi^+$) invariant mass distributions for p-Pb (left) and pp (right)

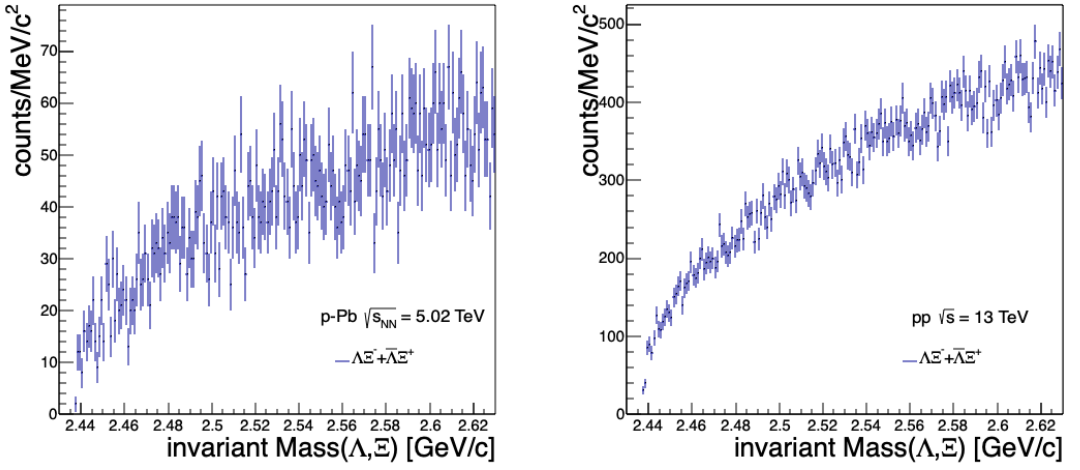

Fig. 4.3: $\Lambda\Xi^-$ ($\bar{\Lambda}\Xi^+$) invariant mass distributions for p-Pb (left) and pp (right)

4.2 Background estimation

For dibaryon searches with unknown signal widths, it is important to understand the background in the reconstructed invariant mass distribution. In this section, we will discuss our considerations for the background in the mass distribution using the p-Pb collision data.

4.2.1 Combinatorial background

The background distribution was initially suggested to be only uncorrected combinatorial pairs by mis-combination. The combinatorial distribution can be evaluated by the event mixing technique. Event mixing is an effective method to reproduce uncorrelated distribution including the detector effects by reconstructing the invariant mass using the particles from different events. In this technique, mixing is done by the events with a similar primary vertex z-position and multiplicity, which have similar detector effects. In the initial analysis, the z-vertex position was classified into four classes of 5 cm intervals in the range of -10 to 10 cm, and the multiplicity into 12 classes of 10 each in the range of 0 to 120. The events in the same class were regarded as similar events.

The $\Lambda\Lambda$ ($\bar{\Lambda}\bar{\Lambda}$), p$\Xi^-$ ($\bar{p}\Xi^+$), and $\Lambda\Xi^-$ ($\bar{\Lambda}\Xi^+$) mass distributions in the same events and the mixed events are shown in the left panel of Figs. 4.4, 4.5, and 4.6. In these figures, the red distribution is the mixed event distribution normalized by the number of pairs in the same event distribution and the blue distribution is the same event distribution. The right panel in Fig. 4.4, 4.5, and 4.6 shows that the ratio of the mixed and same event distributions. A clear discrepancy between them is seen even in the high mass region, where pairs were expected to be completely uncorrelated. Thus, the background distribution with hyperons such as Λ and Ξ cannot be described by a simple event mixing.

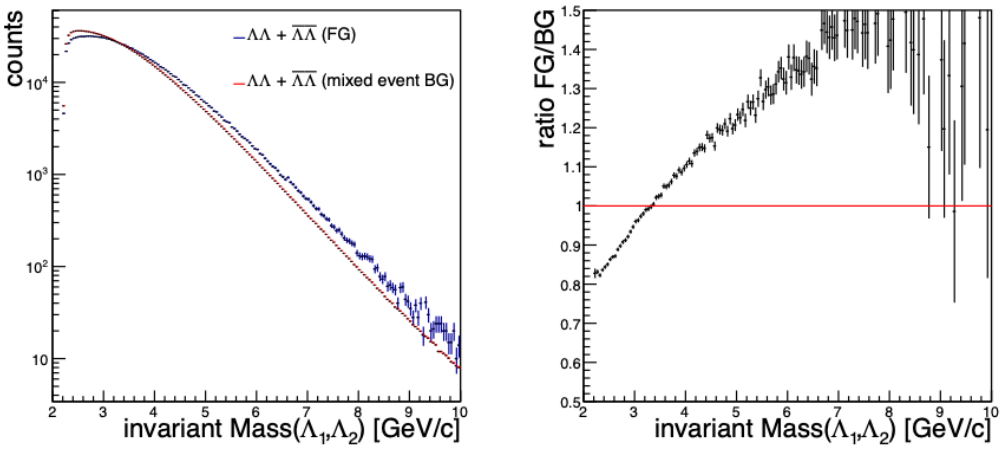

Fig. 4.4: (left) The comparison of $\Lambda\Lambda$ ($\bar{\Lambda}\bar{\Lambda}$) invariant mass distributions in the same events and mixed events (right) The ratio of mixed and same event distributions

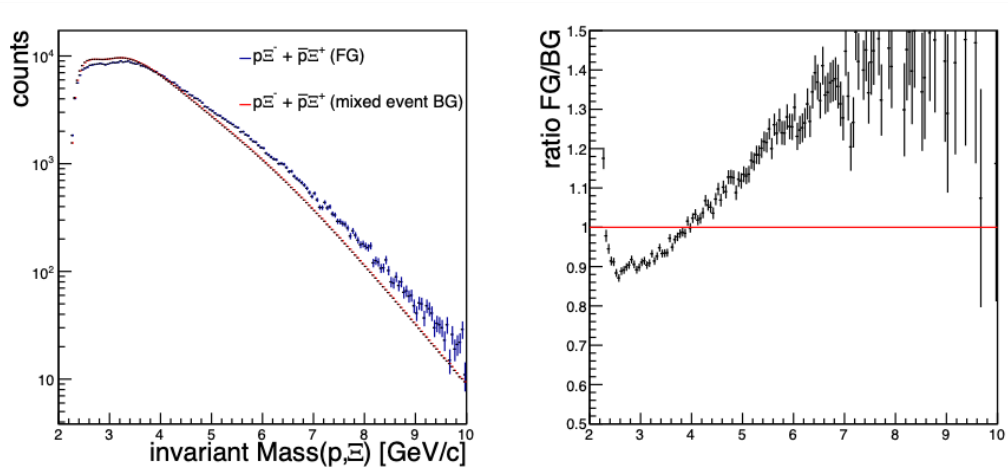

Fig. 4.5: (left) The comparison of $p\Xi^-$ ($\bar{p}\Xi^+$) invariant mass distributions in the same event and mixed event (right) The ratio of mixed and same event distributions

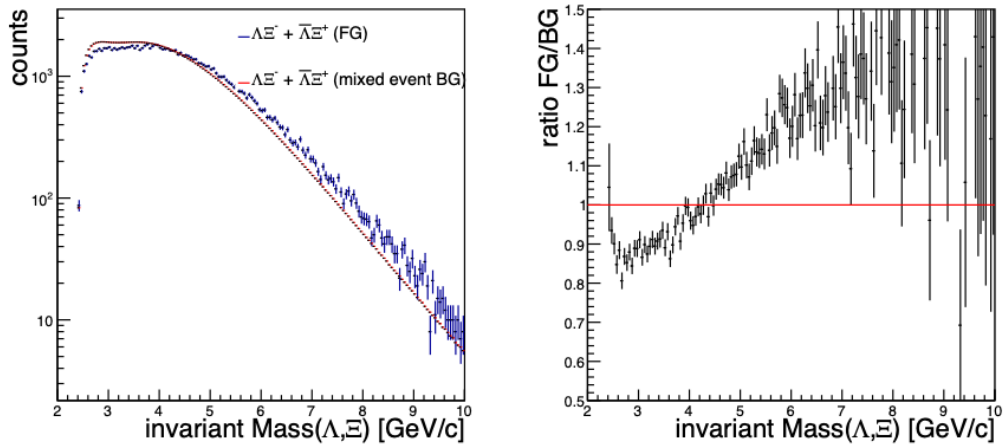

Fig. 4.6: (left) The comparison of $\Lambda\Xi^-$ ($\bar{\Lambda}\Xi^+$) invariant mass distributions in the same event and mixed event (right) The ratio of mixed and same event distributions

Therefore, the criteria of similar events for event mixing were re-defined as follows :

1. Finer segmentation for low multiplicity events
2. Only events where at least one hyperon pair is found

Segmentation of low multiplicity events

Figure 4.7 shows the comparison of the $\Lambda\Lambda$ ($\bar{\Lambda}\bar{\Lambda}$) invariant mass distributions at the same events (blue) and mixed events (red) for different multiplicity classes used in the simple event mixing. The difference between them is more significant in the lower multiplicity classes. Thus, the multiplicity is classified more finely particularly in the low multiplicity region as follows :

- 10 classes for 1 to 40 (4 multiplicity each)
- 8 classes for 41 to 120 (10 multiplicity each)

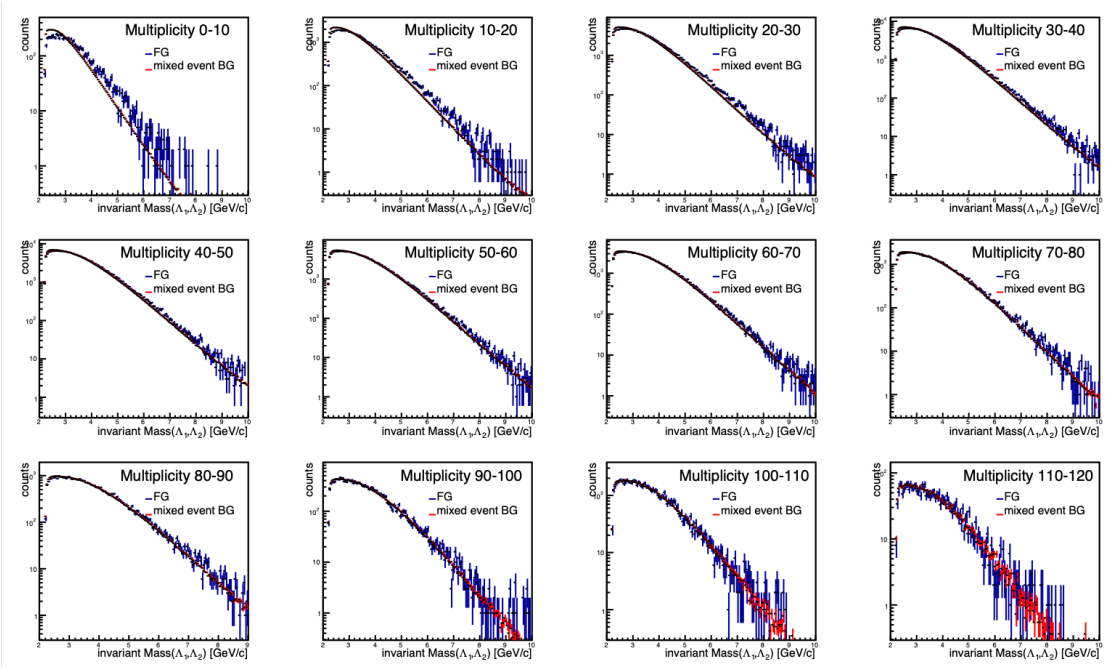

Fig. 4.7: $\Lambda\Lambda$ ($\bar{\Lambda}\bar{\Lambda}$) invariant mass distribution in each multiplicity classes

Consideration for events generated the hyperons

The events containing more than two hyperons are not typical due to smaller cross sections of hyperons than charged particles such as π, K, p. Thus, the events with at least one pair of hyperons one only used for event mixing to ensure the event similarity. After improving the mixed event similarity, $\Lambda\Lambda$ ($\bar{\Lambda}\bar{\Lambda}$), $p\Xi^-$ ($\bar{p}\Xi^+$), and $\Lambda\Xi^-$ ($\bar{\Lambda}\Xi^+$) invariant mass distributions at the same events and mixed events are shown in Figs. 4.8, 4.9, and 4.10. By considering the hyperon multiplicity, their agreement gets more better. The mixed event distribution gets more consistent particularly in the low multiplicity in Fig. 4.11.

These results show that the two changes for mixed events are effective, but there are still differences in low mass region from the ratio plot.

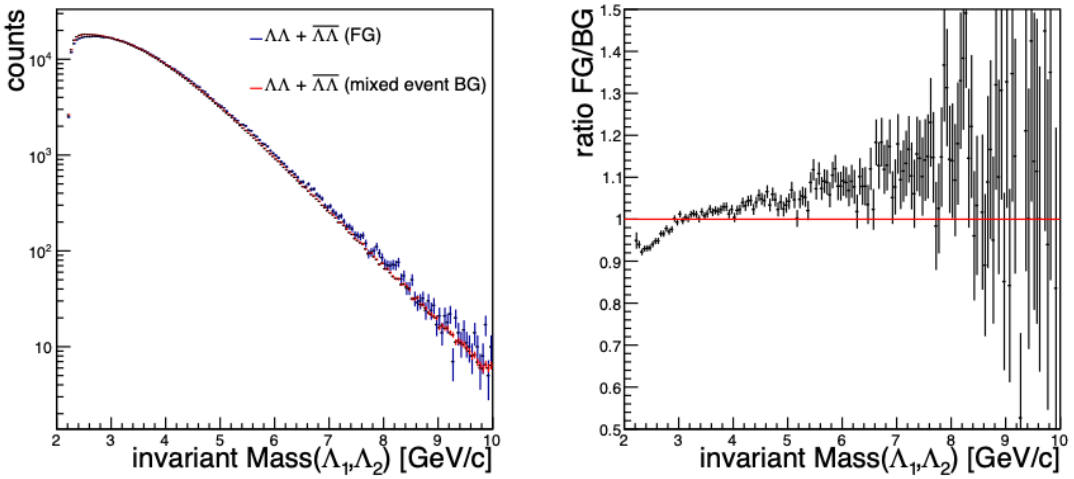

Fig. 4.8: The comparison of $\Lambda\Lambda$ ($\bar{\Lambda}\bar{\Lambda}$) invariant mass distribution at the same event and mixed event after improvement mixed event similarity

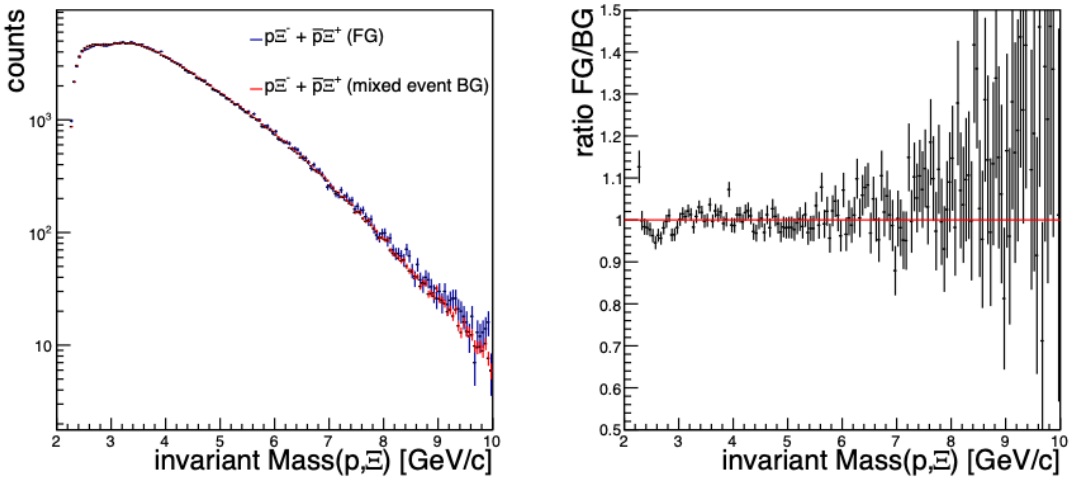

Fig. 4.9: The comparison of $p\Xi^-$ ($\bar{p}\bar{\Xi}^+$) invariant mass distribution at the same event and mixed event after improvement mixed event similarity

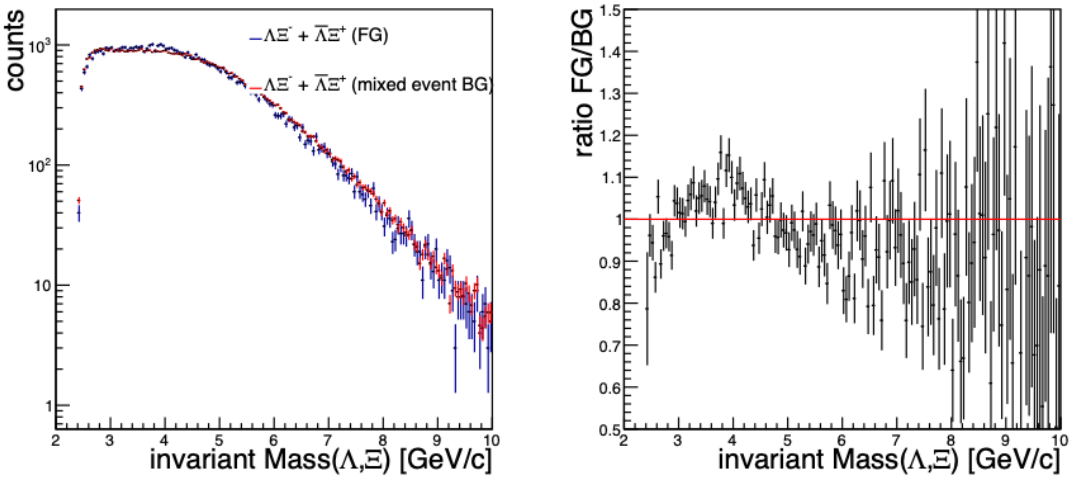

Fig. 4.10: The comparison of $\Lambda\Xi^-$ ($\bar{\Lambda}\bar{\Xi}^+$) invariant mass distribution at the same event and mixed event after improvement mixed event similarity

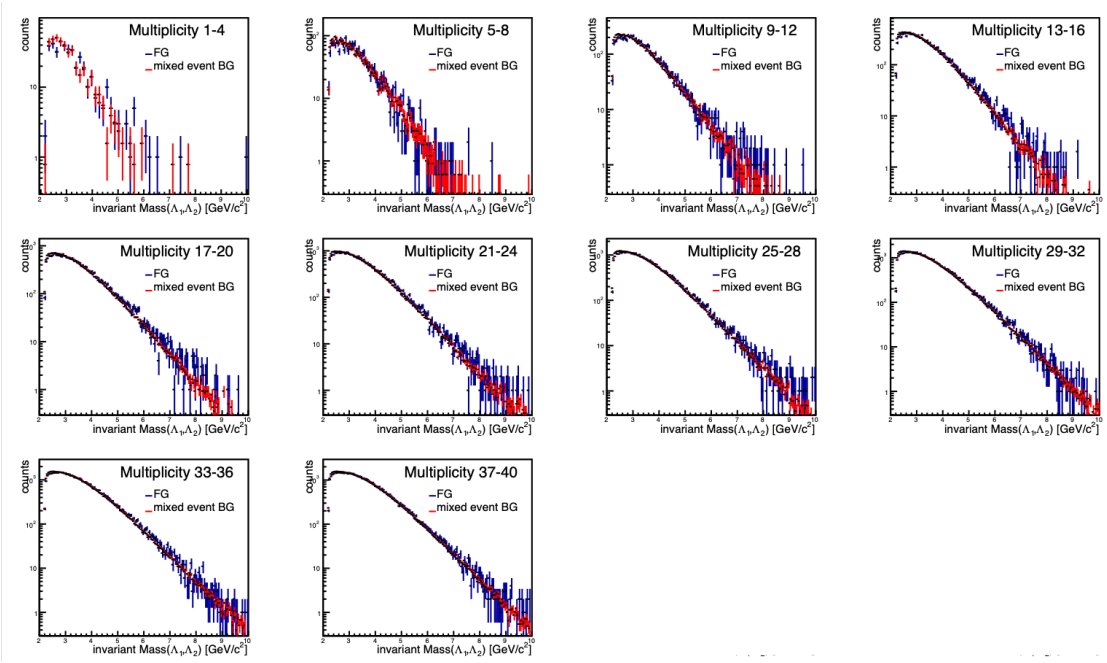

Fig. 4.11: $\Lambda\Lambda$ ($\bar{\Lambda}\bar{\Lambda}$) invariant mass distribution in each multiplicity classes after improvement mixed event similarity

4.2.2 Jet and flow contributions

The remaining difference with the mixed event mass distribution implies other background contributions. Possible contributions are semi-correlated pairs in jet and modulation of combinatorial distribution by elliptic flow. Jets are hadronic populations emitted by high-energy parton scattering of incoming nucleons. The elliptic flow is the azimuthal anisotropy of the particles due to the geometrical feature of a collision. The particles in jet or along with the flow are concentrated in a narrow angular region. Therefore, We have used MC simulations in which jet events generated by the event generator PYTHIA8 are embedded in p-Pb collisions at 5.02 TeV produced by EPOS-LHC, where the effect of flow is taken into account, to evaluate jet and flow contributions.

For $\Lambda\Lambda$ ($\bar{\Lambda}\bar{\Lambda}$) invariant mass distribution in the MC simulation, the MC distribution consists of combinatorial distribution and Jet and flow correlations. The jet and flow correlations can be extracted by the following procedure.

1. Normalize the mass distribution at mixed events in wide angular range where the no effects of jet and flow are expected
2. Subtract the mass distribution at mixed events from the mass distribution at same events in the MC simulation

The step 1 is done to confirm the effect of jet and flow on the mass distribution. Since the particles

produced by jet and flow emit at almost the same angle or back-to-back, the angle between the pairs is narrower. Therefore, particles in the mid-angle region are not affected by jet or flow. In other words, normalizing the mass distribution at mixed events by the number of same event pairs in such a region can be seen the difference in the mass distribution caused by jet and flow effects. In the left panel of Fig. 4.12, the red line show the distribution at same events and the blue line show the normalized distribution at mixed events. This panel shows the difference betweem two distributions. In step2, we can see the shape that jet and flow affect to the mass distribution by considering the residual distribution of these distributions. in the right panel of Fig. 4.12,the residual distributions after subtraction of the normalized mixed event are also shown. This shape, which is a major feature in low mass region, is considered to be the effect of jet and flow on the $\Lambda\Lambda$ mass distribution.

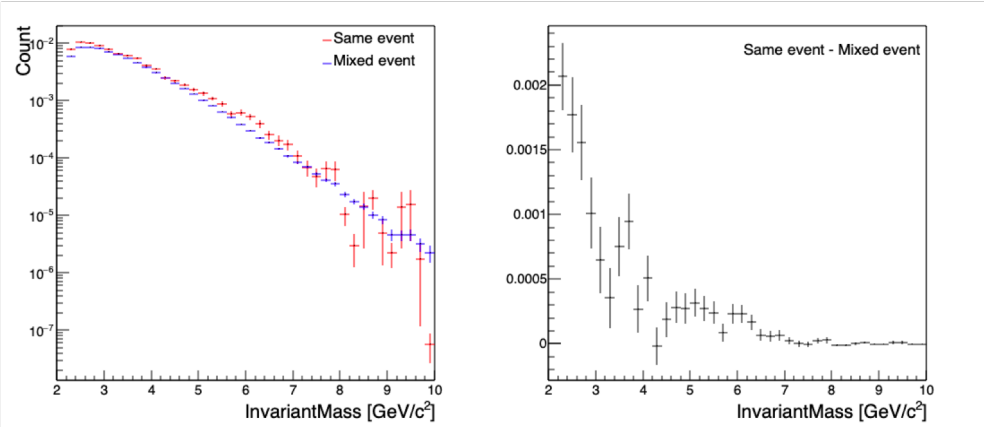

Fig. 4.12: (left) The comparison of $\Lambda\Lambda$ ($\bar{\Lambda}\bar{\Lambda}$) invariant mass distributions at same events and mixed events (right) The invariant mass distributions after subtraction of the mixed event distribution

Finally, in Fig. 4.13, the green distribution indicates that the mass distribution by jet and flow correlation (Fig. 4.12(right)) assumed in real data. The blue distribution shows the combinatorial distribution in real data, and the red distribution shows the addition of the distributions of jet and flow correlation to that distribution. The black distribution shows the mass distribution at same events in real data, and the comparison between this and the red distribution indicate that two distribution is consistent. The results show that the jet and flow correlation in real data has little effect on the distribution.

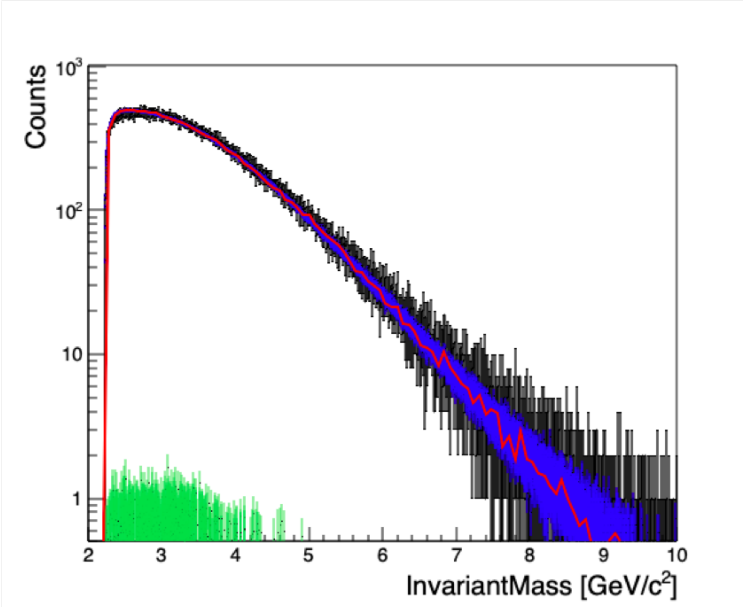

Fig. 4.13: The effect of jet and flow correlation assumed in real data (black) the distribution in real data (green) the distribution by jet and flow correlation in real data (blue) the combinatorial distribution in real data (red) the distribution by jet and flow correlation + the combinatorial distribution in real data

As a consequence of this background estimation, although the reproducibility of the background by event mixing was improved by considering hyperon multiplicity, there is still a discrepancy in the low mass region. Furthermore, MC simulation shows that the discrepancy is not due to jet and flow correlation.

4.3 Evaluation of multi-strange dibaryon signal significance based on statistical hypothesis testing

In this section, the way of the statistical hypothesis tests, which have been performed to set the signal upper limits of the $\Lambda\Lambda$, $p\Xi$, and $\Lambda\Xi$, is described.

4.3.1 CLs method

First, the following hypotheses are considered to search for a possible signals in the obtained data samples:

- Null hypothesis : Observed data consists of background data only
- Alternative hypothesis : Observed data consists of signal and background

Introducing a test statistic

In order to quantify which of the two hypotheses should be rejected by the observed data, the likelihood ratio can be used as a test statistic. Assuming that the two hypotheses follow a Poisson distribution, the likelihood ratio Q can be written as :

$$Q = \frac{e^{-(s+b)}(s+b)^d}{d!} / \frac{e^{-b}b^d}{d!}, \tag{4.1}$$

where, s is the number of signals, b is the number of background, and d is the total number of data points in the observed data. Then, the log likelihood ratio, $log\ Q$, was introduced as:

$$log\ Q = -s + d\ log\ \left(1 + \frac{s}{b}\right). \tag{4.2}$$

In the analysis, the test statistic, $log\ Q$, was calculated for each mass bin and can be expressed as follows.

$$log\ Q = \sum_{i=1}^{n_{bins}} \left\{ -s_i + n_i\ log\ \left(1 + \frac{s_i}{b_i}\right) \right\}. \tag{4.3}$$

In Eq. 4.3, n_{bins} are the number of bins in the data and n_i is the number of entries in bin i.

Definition of confidence level

The confidence level for the alternative hypothesis, CL_{s+b}, is defined as the probability that a value of the test statistic, $log\ Q_{s+b}$, is less than the one with the observed data, $log\ Q_{data}$. In Eq. 4.4, $p(log\ Q|s+b)$ is the probability density function for the alternative hypothesis.

$$CL_{s+b} = \int_{-\infty}^{log\ Q_{data}} p(log\ Q|s+b) dlog\ Q. \tag{4.4}$$

The confidence level for the null hypothesis, $log\ Q_b$, is also defined in the same way for the alternative hypothesis.

$$CL_b = \int_{-\infty}^{log\ Q_{data}} p(log\ Q|b) dlog\ Q \tag{4.5}$$

Figure 4.14 shows an example of the distributions of $p(log\ Q|s+b)$ and $p(log\ Q|b)$ with d = 370, b = 400, and s = 20. The distributions of $p(log\ Q|s+b)$ (blue line) and $p(log\ Q|b)$ (red line) were calculated by randomly generated d samples by Poisson distributions with mean values of $s+b$ and b, then $log\ Q|s+b, b$ are calculated by Eq. 4.3. In this figure, $log\ Q_{data}$ with $d = 370$ is indicated by the grey line around $log\ Q = -2$, and CL_{s+b} and CL_b correspond to the blue and red filled regions, respectively.

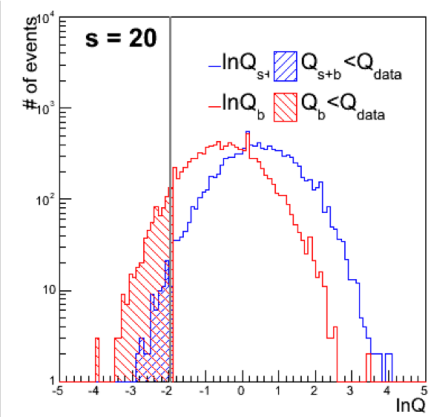

Fig. 4.14: The distributions of $p(log\ Q|s+b)$ and $p(log\ Q|b)$ with d=370, b=400, s=20

Confidence level for signal CLs

In the case of very small signal strength, CL_{s+b} and CL_b can be consistent because the $s+b$ distribution does not differ from the only b distribution. To ensure the $s+b$ distribution can be separated from the only b distribution, an alternative confidence level for a signal is introduced and its definition is

$$CL_s = \frac{CL_{s+b}}{CL_b}. \tag{4.6}$$

Therefore, the $s + b$ hypothesis can be rejected at the confidence level CL = 1 - CLs.

4.3.2 Results of CLs calculation

The dibaryon peak searches have been performed with the CLs calculations. In Tab. 4.3, the signal search regions, the assumed signal widths and the bin widths of the invariant mass distribution are summarized for $\Lambda\Lambda$, $p\Xi$, and $\Lambda\Xi$, respectively. The search signal regions were determined based on the signal region of each dibaryon. A Gaussian distribution with the signal width is assumed as a signal shape. The dibaryon signal widths are unknown, then they are set to be sufficiently larger than bin widths of mass distributions not to be too sensitive to statistical fluctuations of the data points.

pairs	signal search region $(\mathrm{GeV/c^2})$	signal width $(\mathrm{MeV/c^2})$	bin width $(\mathrm{MeV/c^2})$
$\Lambda\Lambda$	[2.23,2.26]	5	1
$p\Xi$	[2.26,2.36]	10	2
$\Lambda\Xi$	[2.44,2.61]	20	4

Tab. 4.3: Target dibaryon's signal search regions, signal widths and mass bin widths for CLs calculation

In this analysis, since the background evaluation (Section 4.2) was not sufficient, a smooth 4th order fit function was used to describe the background in the invariant mass distribution. The fit results of the mass distributions for pp (top) and p-Pb (bottom) data are shown in the left panels of Figs. 4.15, 4.16, 4.17. The blue symbols show the real data and the resulted 4th order polynomial function is indicated by the red dotted line. The residual distributions after subtraction of the fit function from the data are also shown in the right panels. The fit results look consistent with the data. Thus, the background description with the fits was well determined for CLs calculations. It is noted that a possible signal region is included in the background fit, however it does not make any big impact on the background description because the number of signals is considered sufficiently small compared to the background.

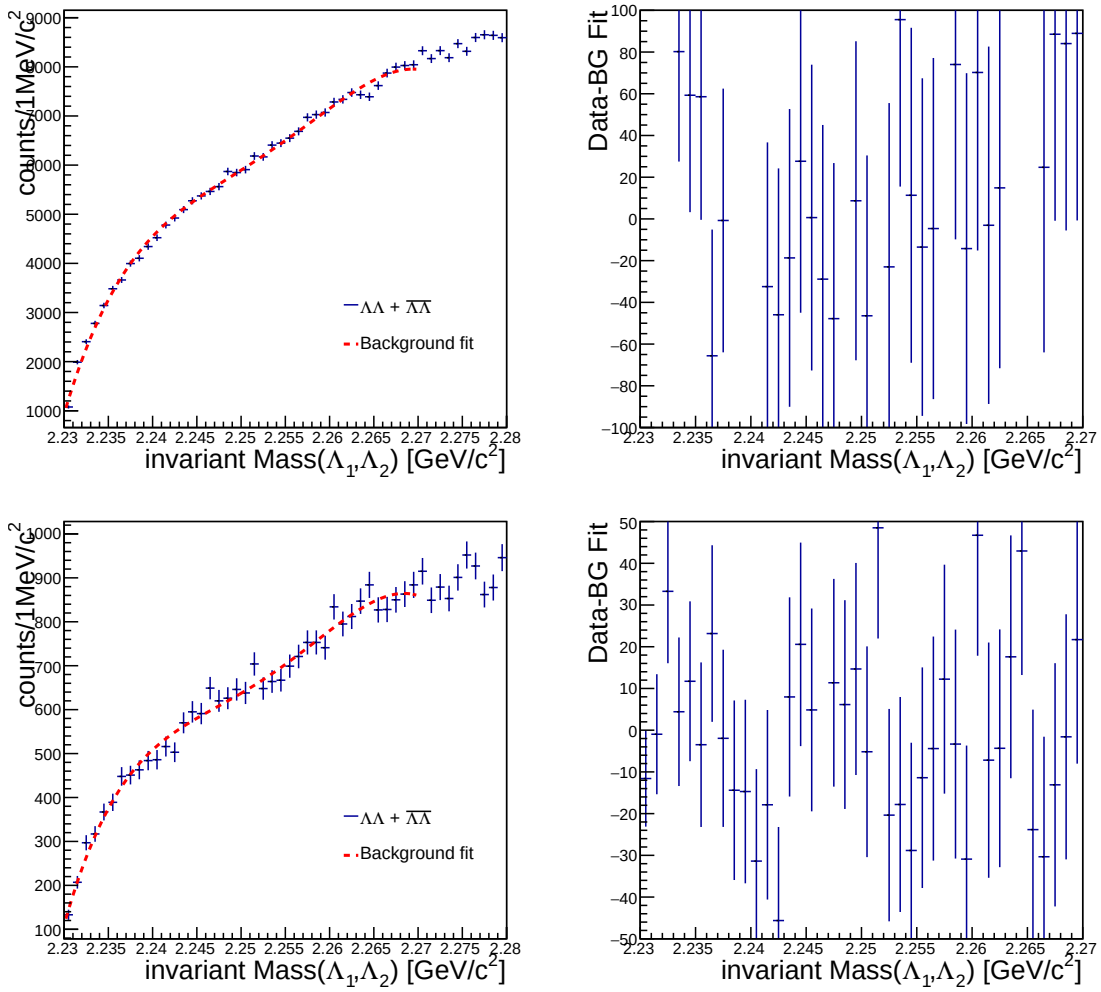

Fig. 4.15: (Left) The fit result of $\Lambda\Lambda$ invariant mass distribution with a 4th order fit function. The real data is indicated by the blue symbols and the fit function is indicated by the red doted line. (Right) The residual distribution after subtraction of the fit function from the data.

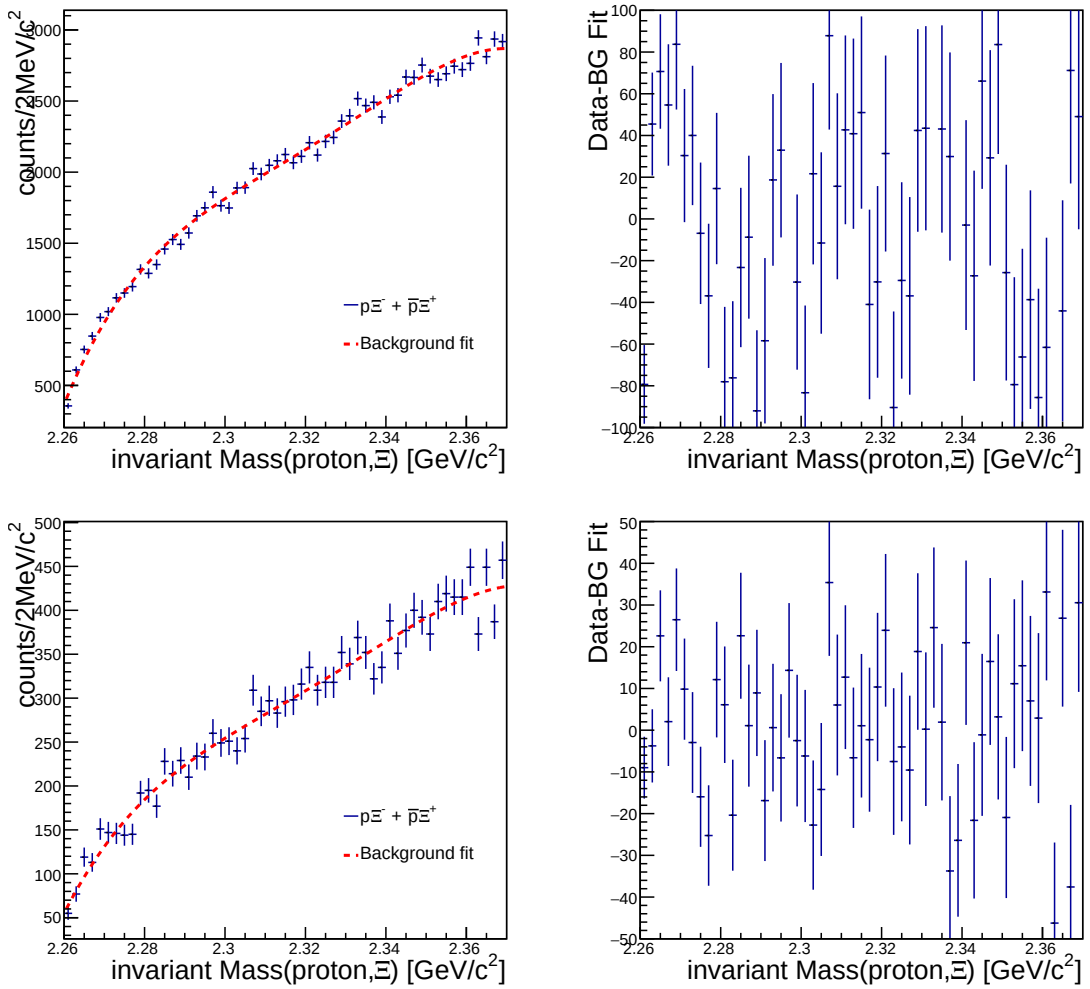

Fig. 4.16: (Left) The fit result of $p\Xi$ invariant mass distribution with a 4th order fit function. The real data is indicated by the blue symbols and the fit function is indicated by the red doted line. (Right) The residual distribution after subtraction of the fit function from the data.

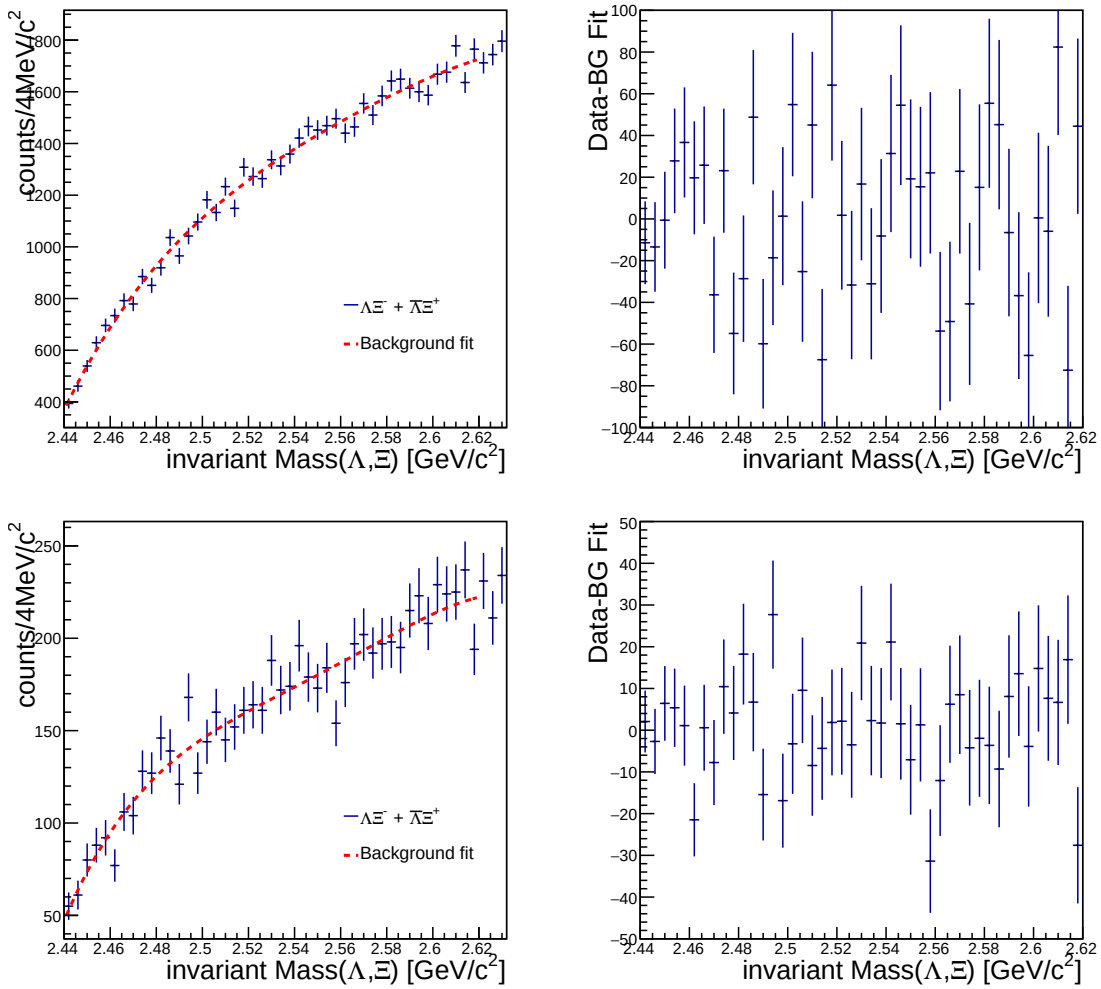

Fig. 4.17: (Left) The fit result of $\Lambda\Xi$ invariant mass distribution with a 4th order fit function. The real data is indicated by the blue symbols and the fit function is indicated by the red doted line. (Right) The residual distribution after subtraction of the fit function from the data.

The number of signals at 90% confidence level for each target dibaryon was calculated with the described signal shape and background for CLs calculations. The results are shown as a function of the bibaryon mass in Figs. 4.18, 4.19, 4.20. The black solid line represents the observed data, the black dotted line represents the experimental sensitivity with the statistics of the hyperon pair samples, and the green and yellow bands represent $\pm 1\sigma$ and $\pm 2\sigma$ uncertainties of the statistical fluctuation of the experimental sensitivity, respectively. The possible signals at 90% confidence level with the data are consistent within $\pm 2\sigma$ uncertainties of the statistical fluctuation for all target bibaryons. Therefore no signal can be found with the assumed signal widths in the analyzed pp and p-Pb data samples.

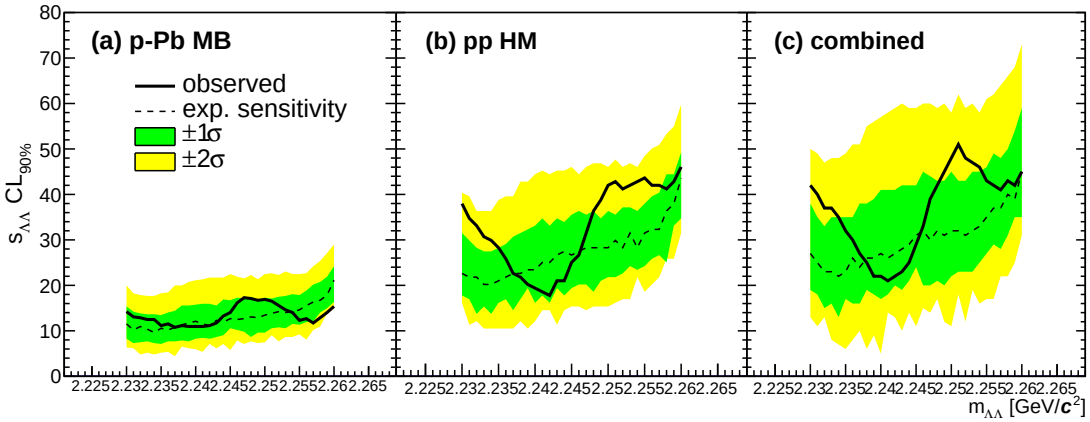

Fig. 4.18: $\mathrm{sCL}_{90\%}$ as a function of the $\Lambda\Lambda$ invariant mass

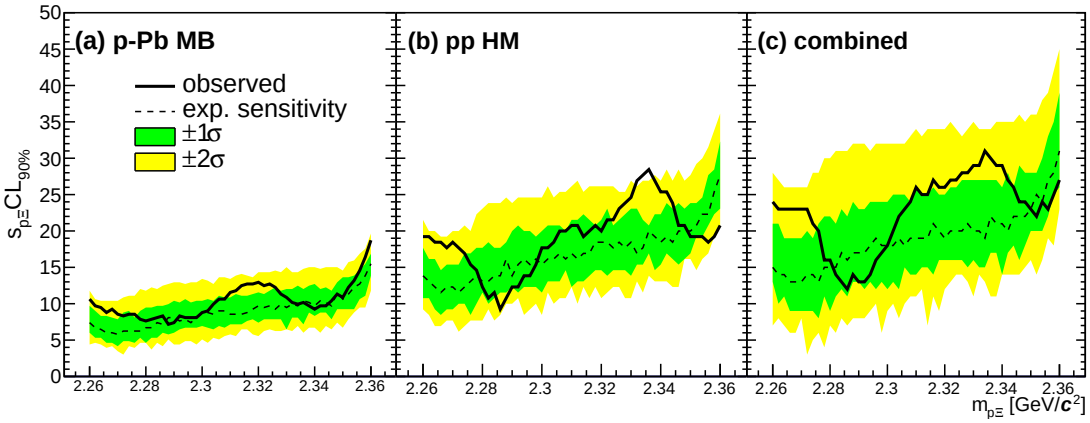

Fig. 4.19: $\mathrm{sCL}_{90\%}$ as a function of the $p\Xi$ invariant mass

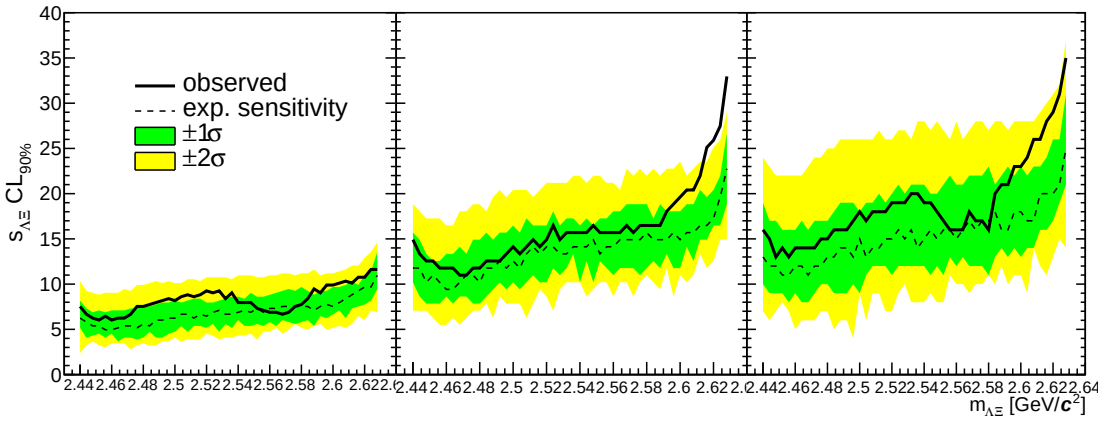

Fig. 4.20: $\mathrm{sCL}_{90\%}$ as a function of the $\Lambda\Xi$ invariant mass

5 Summary

In this study, we have searched for H dibaryon and $N\Omega$ dibaryon using the LHC Run 2 pp and p-Pb collision data obtained by the ALICE experiment. H dibaryon and $N\Omega$ dibaryon have been reconstructed with possible decay particles via $H \rightarrow \Lambda\Lambda$, $p\Xi$ and $N\Omega \rightarrow \Lambda\Xi$. The possible number of signals at 90% confidence level has been evaluated based on the CL_s calculations with the reconstructed mass distribution of $\Lambda\Lambda, p\Xi$ and $\Lambda\Xi$. As a result, no significance above 2σ uncertainty of the experimental sensitivity due to a statistical fluctuation is observed assuming their signal widths are 5, 10 and 20 MeV/c^2, respectively.

In addition, we were not able to search for $\Omega\Omega$ which is known to be another leading multi-strange dibaryon candidate due to a lack of the statistics. The expected statistics taken in the LHC Run 3 starting from April, 2022, is more than 50 times larger than the current statistics. Therefore the search for all leading multi-strange dibaryon candidates including $\Omega\Omega$ can be realized soon.

References

[1] P.A. Zyla et al. (Particle Data Group), Prog. Theor. Exp. Phys. 2020, 083C01 (2020)

[2] H. Yukawa, Physico-Mathematical Society of Japan, 17 (1935) 48-57.

[3] Cecil Frank Powell, Nature 160, 453(1947).

[4] M. Gell-Mann, Phys. Lett. 8, 214 (1964).

[5] G. Zweig, CERN-TH-401, CERN-TH-412, NP-14146, PRINT-64-170 (1964).

[6] Tanmoy Chakraborty, Tanay Kibe, Sunny Kumar Singh,, Department of Physics, IIT Madras, Chennai-600036.

[7] .A. Zylaet al.(Particle Data Group), Prog. Theor. Exp. Phys.2020, 083C01 (2021) and 2021 update1st December, 2021 8:56am.

[8] S. K. Choi et al. (Belle), Phys. Rev. Lett. 91, 262001 (2003).

[9] 51. B. Aubert et al. (BaBar), Phys. Rev. Lett. 95, 142001 (2005).

[10] R. Aaij et al. (LHCb), Phys. Rev. Lett. 115, 072001 (2015).

[11] Ishii, Aoki, Hatsuda, Phys. Rev. Lett.99, 022001(2007).

[12] R. Hanbury Brown and R. Q. Twiss, Nature 178, 1046 (1956).

[13] ALICE Collaboration, Nature volume 588, pages 232 – 238 (2020).

[14] RL Jaffe, Phys. Rev. Lett.38, 617(1977).

[15] ALICE Collaboration, Physics Letters B, Volume 752, Pages 267-277(2016).

[16] ALICE Collaboration, Physics Letters B, Volume 797, 134822(2019).

[17] ALICE Collaboration, Phys. Rev. B 797, 134822 (2019).

[18] ALICE Collaboration, Phys. Rev. Lett. 123, 112002 (2019).

[19] HAL QCD Collaboration, Physics Letters A, Volume 881, Pages 28-43(2012).

[20] Takumi Iritani, Sinya Aoki, Takumi Doi, Faisal Etminan, Shinya Gongyo, Tetsuo Hatsuda, Yoichi Ikeda, Takashi Inoue, Noriyoshi Ishii, Takaya Miyamoto, Kenji Sasaki, Phys. Lett. B792, 284-289(2019).

[21] ALICE Collaboration, Nature Physics volume 13, pages 535 – 539 (2017).

[22] ALICE Collaboration, Nature Physics volume 561, pages 321 – 330 (2018).

[23] http://cds.cern.ch/images/OPEN-PHO-ACCEL-2013-056-1

[24] https://home.cern/resources/faqs/facts-and-figures-about-lhc

[25] https://home.cern/science/accelerators/accelerator-complex

[26] https://alice-collaboration.web.cern.ch

[27] https://home.cern/science/experiments/alice

[28] ALICE Collaboration, International Journal of Modern Physics AVol. 29, No. 24, 1430044 (2014).

[29] https://cds.cern.ch/record/1129812/files/jinst8 __ 08 __ s08002.pdf

[30] https://www.ibspe.com/news/alice-prepares-for-run-3-after-last-new-subdetector-installation

[31] https://alice-collaboration.web.cern.ch/menu __ proj __ items/its

[32] B Abelev et al.and The ALICE Collaboration, Journal of Physics G: Nuclear and Particle Physics, Volume 41, Number 8.

[33] http://www.npr.ac.cn/fileYZHWLPL/journal/article/yzhwlpl/2020/3/PIC/2019-CNPC51-2.jpg

[34] https://alice-collaboration.web.cern.ch/node/34960

[35] G.Dellacasaetal.[ALICECollaboration], ALICE technical design report:Time projection chamber (TPC), CERN-LHCC-2000-01, ALICE TDR 7(2000).

[36] Andreas Mathis, EPJ Web Conf, Volume 174(2018)

[37] G. Dellacasa et al. [ALICE Collaboration], ALICE technical design report of the time of flight system (TOF), CERN-LHCC-2000-12, ALICE TDR 8(2000).

[38] ALICE Collaboration, The European Physical Journal Plus 132, Article number: 99 (2017).

[39] https://alice-collaboration.web.cern.ch/menu __ proj __ items/ZDC

[40] http://cds.cern.ch/record/630193

[41] ALICE Collaboration, ALICE technical design report on Forward Detectors: FMD, T0 and V0, CERN-LHCC-2004-025, ALICE-TDR-011(2004)

[42] M. Tanabashi et al. (Particle Data Group), Phys. Rev. D 98, 030001 (2018) and 2019 update 6th December.

[43] ALICE Collaboration, Phys. A 29, 1430044 (2014).

[44] A. Akindinov et al., Eur. Phys. J. Plus 128, 44 (2013).

[45] T. Pierog, Iu. Karpenko, J. M. Katzy, E. Yatsenko, and K. Werner, Phys. Rev. C 92, CERN-LHCC-2004-025, 034906(2015).

Acknowledgment

First of all, I would like to thank all the people who were involved in my research. My supervisor, Professor Kenta Shigaki, gave me a lot of advice on my research. You have been taking care of me since I was a fourth-year undergraduate student, and I probably caused you a lot of trouble. I would like to thank you for your efforts in helping me to successfully complete my master thesis. I would like to thank my mentor, Associate Professor Yorito Yamaguchi, for his great support from the time I started my research until the very end of my master's thesis. I think I caused a lot more trouble for you. But it would be nice if you could be a little more gentle. I would also like to thank all the staff in the lab. I would like to thank Associate Professor Kensuke Homma for discussing my research in the meeting. I respect you for always doing his best. Assistant Professor Takahiro Miyoshi was always kind to me. I would like to talk with you more, as I don't usually get the chance. Assistant Professor Satoshi Yano has taught me a lot about analysis. At first I was very scared of you, but now I rely on you a lot. Researcher Masanori Ogino gave me good advice on how to make slides. Your friendly atmosphere is very nice.

Thank you to everyone in C220 for playing with me so much, it was a great memory even though we talked all day and sometimes I couldn't research. Thank you to all the other students.

Finally, I would like to thank my family for supporting my student life.